# UAV-based method for measuring $CO_2$ emissions in forest ecosystems

Haijiong Sun[1], Shao-Meng Li[1*], Yifei Wang[3], Yanrong Yang[4], Tianran Han[5], Keyu Chen[1], Chang Liu[1], Jietao, Zhou[1], Zeqing Ma[2], Fengting Yang[2], Junfei Guo[6], Xiangyu Gao[6]

[1] College of Environmental Sciences and Engineering, Peking University, Beijing 100871, China

[2] Qianyanzhou Ecological Research Station, Key Laboratory of Ecosystem Network Observation and Modeling, Institute of Geographic Sciences and Natural Resources Research, Chinese Academy of Sciences, Beijing 100101, China

[3] Inner Mongolia Institute of Metrology and Testing, Hohhot 010060, China

Key Lab. for Restoration and Reconstruction of Degraded Ecosystems in Northwestern

[4] China of Ministry of Education, School of Ecology and Environment, Ningxia University, Yinchuan 750021, China

[5] China Electric Power Research Institute, Beijing 100192, China

[6] Beijing Wisdominc Technology Co., Ltd, Beijing 100070

* Correspondence to: Shao-Meng Li (shaomeng.li@pku.edu.cn)

# Abstract

This study addresses the difficulty of accurately quantifying $CO_2$ emissions in forest ecosystems due to spatial heterogeneity, complex terrain, and the combined effects of horizontal and vertical transport. A UAV-based flux quantification methodology, capable of three-dimensional $CO_2$ emission computation, was developed, evaluated and applied to a forest ecosystem. The UAV system is integrated with a high-precision closed-path $CO_2$ analyzer to measure $CO_2$ mixing ratios and a calibrated ultrasonic anemometer to measure wind vectors, together with profile measurements of temperature and pressure. Within a mass-balance framework, the UAV measurement system is flown along horizontal loops at multiple heights together with vertical ascent flight tracks, acquiring data along the flight tracks that are used to simultaneously quantify horizontal advective and vertical turbulent carbon dioxide emission components. The method was applied at a subtropical plantation forest and evaluated against a collocated eddy-covariance (EC) flux tower. Validation against a long-term flux tower shows that vertical $CO_2$ fluxes derived using the gradient method agree well with EC observations across seasons, with a correlation coefficient $r$ of 0.9. Horizontal measurements further reveal pronounced local canopy air diurnal $CO_2$ mass flux variation: lateral advection dominates in the early morning, whereas vertical uptake prevails under well-mixed midday conditions. Sensitivity analysis of emission intensities across multi-scale grid boxes (50×50×50 $m^3$, 100×100×50 $m^3$, and 150×150×50 $m^3$) revealed stronger scale dependence during autumn mornings, indicating significant spatial heterogeneity in $CO_2$ emissions. Uncertainty assessment suggests that the total relative uncertainty of UAV-derived emissions is typically ~22%, with wind-field measurement as the main error source. Overall, this UAV approach provides a flexible and reliable method for analyzing near-surface three-dimensional $CO_2$ transport over complex and heterogeneous forests, helping to overcome the limited spatial coverage of traditional flux towers and remote sensing.



**Keywords:** UAV-based observations; $CO_2$ emissions; Mass balance; Three-dimensional flux measurement; Spatial heterogeneity

# 1 Introduction

Carbon dioxide ($CO_2$) is the dominant anthropogenic greenhouse gas in the atmosphere, contributing approximately 50–60% to the enhanced greenhouse effect excluding water vapor (WMO, 2023). Atmospheric $CO_2$ budget, however, is strongly impacted by biospheric carbon cycles. Forest ecosystems, in particular, play a critical role in the terrestrial carbon cycle and are widely recognized as major carbon sinks, covering about 40% of the global land surface and representing some of the most extensive and structurally complex ecosystems on Earth (Bonan, 2008; IPCC, 2021; Pan et al., 2011). Accurate quantification of forest-atmosphere carbon exchange remains essential for constraining regional and global carbon budgets and for evaluating ecosystem feedbacks from climate change. Recent synthesis studies and observation-network analyses continue to highlight the importance of improving carbon flux measurements across heterogeneous ecosystems (Fang et al., 2024; Burman et al., 2025). However, despite decades of carbon-cycle research aimed at estimating $CO_2$ exchange across spatial scales using a variety of observational platforms, including stationary towers, satellite-based remote sensing, and manned aircraft measurements (Baldocchi, 2003; Gioli et al., 2004; Jung et al., 2020), most existing methods are inherently confined to either vertical or horizontal dimensions due to theoretical or practical limitations, which restrict their ability to represent the full three-dimensional structure of $CO_2$ transport in the lower atmosphere (Leuning et al., 2008). In forest ecosystems, strong spatial heterogeneity, complex canopy-atmosphere interactions, and non-negligible horizontal transport processes can introduce substantial uncertainties into quantitative estimates of ecosystem-atmosphere $CO_2$ exchange (Baldocchi, 2008; Schimel et al., 2015). As a result, approaches capable of resolving both horizontal and vertical $CO_2$ transport are required.

Eddy covariance (EC) flux measurement technique is currently the most widely used method (Aubinet et al., 2012; Baldocchi, 2003; Burman et al., 2025; Pastorello et al., 2020; Fang et al., 2024) for quantifying ecosystem-scale vertical $CO_2$ fluxes and has been implemented globally through networks such as the FLUXNET (Aubinet et

al., 2012; Baldocchi et al., 2001; Fang et al., 2024; Pastorello et al., 2020; Wilson et al., 2002). By design, EC provides direct measurements of time-averaged vertical turbulent flux of $CO_2$ between the surface and the atmosphere. However, the method relies on the validity of the Monin–Obukhov Similarity Theory (MOST), which assumes a horizontally homogeneous, flat terrain and stationary turbulence (Foken, 2008; Kaimal and Finnigan, 1994; Monin and Obukhov, 1954; Stull, 1988). Over complex terrain and heterogeneous surfaces, these assumptions are often violated, calling into question the representativeness of EC flux measurement results over such ecosystems. EC flux measurements do not explicitly resolve horizontal $CO_2$ transport associated with advection, canopy heterogeneity, terrain-induced flows, or mesoscale circulations (Aubinet et al., 2002; Feigenwinter et al., 2004; Finnigan et al., 2003; Leuning et al., 2005). Horizontal fluxes are therefore commonly neglected or assumed to be negligible in EC flux measurements, an assumption that may not hold under weak or non-stationary turbulence conditions (Mahrt, 1998, 2010; Vickers and Mahrt, 1997). In addition, stationary towers (e.g. EC flux towers) provide flux information at a fixed height, limiting their ability to characterize $CO_2$ transport at different levels within the atmospheric boundary layer (Schmid, 2002), hence unable to determine flux divergence. For large scale atmosphere-ecosystem $CO_2$ exchanges, satellite remote sensing offers valuable information on horizontal distributions of atmospheric pollutants (Crisp et al., 2017; Jacob et al., 2016), but it has limited sensitivity to vertical gradients near the surface and cannot resolve canopy-scale exchange processes with the accuracy of in situ measurements (Chevallier et al., 2014). Likewise, manned aircraft campaigns provide regional-scale observations of pollutants distributions and enable mass-balance approaches to emission estimation (Cambaliza et al., 2014), but vertical fluxes are difficult to determine (Gordon et al., 2015). Collectively, these limitations highlight a persistent observational gap in the characterization of $CO_2$ three-dimensional transport in forest ecosystems (Fang et al., 2024; Bolek et al., 2024).

Recent advances in rotating wing unmanned aerial vehicle (UAV) platforms and lightweight sensor technologies have created new opportunities for atmospheric

measurements over complex environments (Bolek et al., 2024). UAVs have emerged as practical tools for complementing existing carbon observation networks by enabling flexible, high-resolution measurements of greenhouse gases in both horizontal and vertical directions (Bolek et al., 2024; Khan et al., 2012; Villa et al., 2016). Compared with stationary towers, UAVs can directly measure concentration spatial variability over short time and spatial scales without relying on assumptions of horizontal homogeneity (Witte et al., 2017), enabling identification of emission or uptake hotspots that may be missed by ground-based observations (Khan et al., 2012). Nonetheless, these UAV applications have not demonstrated the feasibility of $CO_2$ flux measurements owing to their inability to conduct accurate wind speed measurements, both of which can be affected by propeller-induced airflow disturbances (Soltaninezhad et al., 2025; Thielicke et al., 2021) and rapidly changing UAV attitude during flight (e.g., variations in pitch, roll, and yaw angles) (Yang et al., 2024), thereby introducing additional uncertainty into the flux calculation. To address these challenges, various sensors, including multi-hole probes, pitot tubes, and sonic anemometers, have been deployed on UAVs for wind measurements and correction algorithms have been developed to mitigate measurement disturbances associated with rotor downwash, re-orientation of airflow by platform geometry, and rapid changes in UAV motion and attitude (Langelaan et al., 2011; Niedzielski et al., 2017; Nolan et al., 2018; Rogers and Finn, 2013; Soddell et al., 2004; Soltaninezhad et al., 2025; Spiess et al., 2007; Yang et al., 2024). Among these, sonic anemometers are considered particularly promising because of their high accuracy and fast response (Thielicke et al., 2021). Nevertheless, the influence of rotor-induced flow distortion, UAV attitude changes, and local turbulence on wind measurements remains non-negligible and requires dedicated calibration strategies (Soltaninezhad et al., 2025; Yang et al., 2024).

Building on our previous work on the development of an UAV platform for integrated high sensitivity, high precision, fast response measurements of greenhouse gas concentrations and three-dimensional wind speed, combined with a comprehensive wind calibration algorithm to correct for UAV motion, attitude, and rotor effects (Yang

et al., 2025), we aim to improve quantification of atmospheric $CO_2$ transport in both horizontal and vertical directions over forest ecosystems. In the present study, we use observations collected with the UAV platform to evaluate the performance of the wind correction algorithm, assess the capability of the integrated UAV measurement system to quantify three-dimensional $CO_2$ transport, including canopy-scale vertical $CO_2$ fluxes, and characterize the robustness and uncertainty of the UAV-derived emission/uptake estimates. The evaluation is based on specifically designed flight strategies with complementary box and profile flight patterns and is conducted in field experiments at a subtropical forest site. Such flight strategies are implemented within a mass-balance framework to resolve three-dimensional $CO_2$ exchange in the lower atmosphere. While horizontal mass flux estimates derived from this platform have been previously evaluated and validated in field measurements (Han et al., 2024) vertical fluxes derived from such a platform have not been evaluated until now, and a critical part of the present study is to validate the UAV vertical flux measurement methodology against the collocated tower-based EC flux measurements. As presented further below, the results demonstrate a highly versatile methodology for determining net carbon fluxes over complex ecosystem terrains that complements existing carbon flux tower measurements by providing spatially explicit information on three-dimensional $CO_2$ transport and, with sufficient UAV observations, an independent estimate of forest carbon fluxes.

# 2 Field site and platform description

## 2.1 Platform description

### 2.1.1 UAV platform

The UAV platform used in this study is a battery-powered hexacopter (KWT-X6L-15, ALLTECH, China), which provides stable flight performance and high maneuverability, including vertical take-off and landing, hovering, and controlled horizontal flight (Fig. 2b). This airframe was selected as the base platform for $CO_2$ measurements because of its ability to operate safely above forest canopies, its high

payload capacity, and its adaptability to multiple flight strategies. The UAV has a maximum horizontal span, including the arms and rotor blades, of 2570 mm, and the height from the landing gear to the top of the main body is 565 mm, excluding the air inlet. Its maximum horizontal flight speed is 18 m $s^{-1}$, the maximum ascending rate is 4 m $s^{-1}$, and the maximum wind resistance is 14.4 m $s^{-1}$, all of which satisfy the requirements for atmospheric wind and $CO_2$ measurements in the lower boundary layer. A detailed summary of the UAV specifications is provided in Table 1.

**Table 1.** Specifications and capabilities of the UAV.

| | |
|---|---|
| hover endurance | ≥30 min (for 15 kg payload) |
| Peak flight velocity | 18 m $s^{-1}$ |
| Peak climb velocity | 4 m $s^{-1}$ |
| Control radio range | ≥7 km |
| Operating ambient temperature | -20 ℃~55 ℃ |
| Maximum operating altitude | ≥5000 m |
| Wind resistance capability | 14.4 m $s^{-1}$ |
| Payload capacity | 15 kg (without battery) |
| Rotor blade length | 765±5 mm |
| Symmetric motor center-to-center length | 1635±10 mm |
| Body stands to the body top length | 565 ± 5 mm |
| Wing span | 2570 ±10 mm |
| Battery capacity/unit | 30000 mAh (2 units) |
| Battery weight/unit | 6 kg ± 0.1 kg |
| Radio modem | 902 MHz ~928 MHz |
| GPS accuracy | Horizontal direction: ± $(8+1\times10^{-6}D)$ mm; Vertical direction: ± $(15+1\times10^{-6}D)$ mm |
| Navigation | GPS (RTK system) |

**Note:** In the GPS accuracy specification, $D$ is the baseline distance between the UAV receiver and the RTK base station, expressed in kilometers.

The airframe is constructed from carbon-fiber composite materials and houses an integrated flight control system, a power supply module, and a communication unit. The flight control system includes an inertial measurement unit (IMU), accelerometers, and a global positioning system (GPS) sensor capable of real-time kinematics (RTK), and records UAV attitude and motion parameters (roll, pitch, yaw, and three-axis accelerations) which is critical for subsequent wind-speed correction. To improve

positioning accuracy, the onboard RTK GPS receiver takes in real-time signals from a concurrently ground-deployed kinematic (RTK) GPS system (iRTK10, Hi-Target, China) for real time computation for centimetre- to millimetre-level accuracies in both the horizontal and vertical directions, which are particularly advantageous over a complex terrain. The power module consists of two lithium–polymer batteries connected in parallel, each with a capacity of 30,000 mAh, enabling a maximum payload of 15 kg and a typical flight endurance of approximately 30 min. The communication module operates in the 890-960 MHz frequency band, allowing reliable telemetry and control within a range of up to 10 km.

### 2.1.2 Scientific payloads

The integrated scientific payloads, with a total weight of 6.35 kg including the mounting chassis, were powered directly by the main UAV batteries. The payloads include a closed-path $CO_2$ analyzer and a 3-d ultrasonic anemometer, with their specifications summarized in Table 2. The 3-d ultrasonic anemometer (Trisonica Mini, LI-COR Environment, USA) is a compact sensor, with a measurement path of 35 mm and a mass of 50 g, that measures three-dimensional wind speeds under its own coordinate system, air temperature, and pressure. The anemometer was mounted 70 cm above the rotor plane to minimize flow distortion caused by propeller blade downwash (Fig. 2b) (Yang et al., 2025). This configuration has been shown to achieve acceptable accuracy (±2%) in previous validation studies using reference-grade meteorological instruments (Palomaki et al., 2017; Shimura et al., 2018; Thielicke et al., 2021). The $CO_2$ analyzer (MIRA Ultra $N_2O$/ $CO_2$, Aeris Technologies, USA) was mounted beneath the UAV body to measure $CO_2$ volume mixing ratios in air, with its air inlet set next to the anemometer sonic sensors to ensure spatially consistent wind and $CO_2$ concentration measurements. The MIRA analyzer operates in the mid-infrared (MIR) spectral range, where $CO_2$ absorption is substantially stronger than in the near-infrared, enabling a high sensitivity within a compact optical cell. A fixed time lag of 5 s, associated with air residence time in the sampling line, was applied to synchronize the $CO_2$ measurements with the wind data.

Data from all scientific payloads, together with UAV attitude and flight parameters (roll, pitch, yaw, three-axis accelerations, and GPS position), were recorded by the onboard main controller via UART communication and stored on an SD card (Fig. 1). In addition, real-time telemetry, including sensor status, battery voltage, and flight parameters, was transmitted to a ground station, allowing continuous monitoring during flight operations. $CO_2$ sampling was performed through the analyzer's built-in sampling ports and internal pump. The $CO_2$ measurements were recorded at 1 Hz, while the anemometer data were recorded at 5 Hz.

**Table 2.** Detailed information of scientific payloads (provided by the manufacturers).

| Instrument | Sample Frequency (Hz) | Weight (kg) | Measurement | Sensitivity or Accuracy |
|---|---|---|---|---|
| MIRA Ultra | 1 | 6 | $CO_2$ | < 200 ppb/s (Sensitivity) |
| Trisonica Mini | 5 | 0.05 | Wind speed | (0 - 10 m/s): ±0.2 m/s |
| | | | | (11 - 30 m/s): ±2% |
| | | | Wind direction | ± 1.0° |
| | | | Temperature | ± 2.0 ℃ |
| | | | Pressure | ± 1.0 kPa |

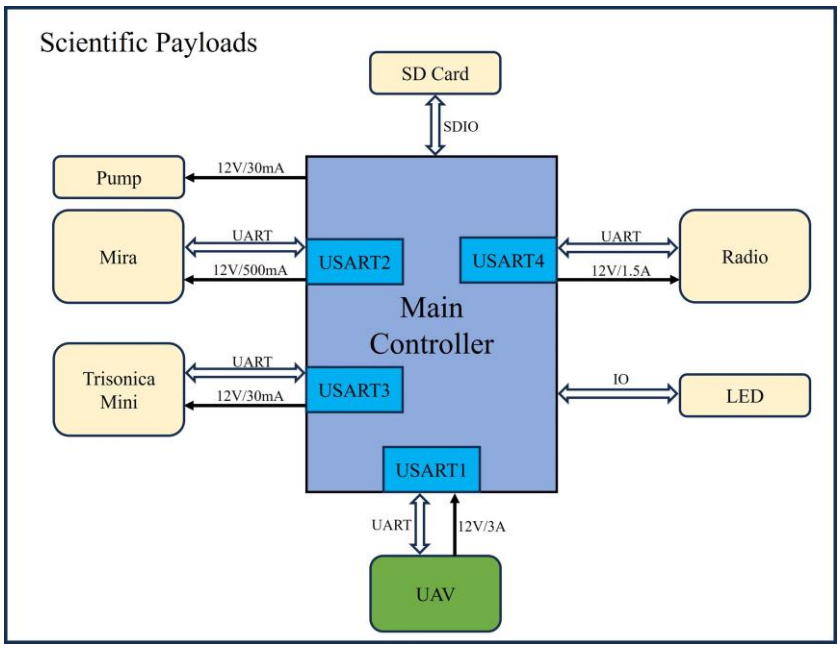



**Figure 1.** Diagram of the scientific payloads on the UAV-based flux measurement system. The LED is used as a status indicator to display the operating state of the UAV measurement system

during flight and ground testing.

## 2.2 Field site description

The UAV-based field measurements were conducted at the Qianyanzhou Experimental Station (26°44′29″ N, 115°03′29″ E) located in Jiangxi Province, southern China. This station is one of the core flux observation sites of the China Flux Observation Research Network (ChinaFLUX) and is equipped with a comprehensive eddy covariance (EC) measurement system (Yu et al., 2006). The flux tower has a height of approximately 43 m above ground, with the EC system installed at 31 m above ground level, while the mean forest canopy height is about 18 m.

The long-term observation site, 1 ha in size and centred on the flux tower, is dominated by plantation forests, primarily consisting of *Pinus massoniana*, *Cunninghamia lanceolata*, and *Pinus elliottii* arranged in a strip-mixed pattern with an approximate ratio of 49:48:3, respectively (Huang et al., 2007). The region experiences a typical subtropical monsoon climate, characterized by prevailing southerly winds in summer and northerly winds in winter. The mean annual air temperature is 17.9 °C, and the mean annual precipitation is approximately 1490 mm, with most rainfall occurring between March and June.

To evaluate the performance of the UAV platform for $CO_2$ vertical flux measurements, measurement flights were conducted at Site B, located approximately 160 m southeast of the flux tower (Site A), and direct comparisons with tower-based measurements were performed (Fig. 2a). Based on a comprehensive site survey, Site B was selected as the UAV take-off and landing location because of its relatively open forest structure, complex surrounding vegetation, and a lower elevation (~15 m lower) than Site A, which facilitates safe UAV operations. Within a radius of approximately 350 m northwest of Site B, only a limited number of low-rise buildings below the forest canopy used exclusively for scientific research are present, resulting in minimal anthropogenic influence on the measured $CO_2$ fluxes. Such an experimental condition provides a representative forest ecosystem setting in which UAV-derived fluxes can be evaluated against flux tower observations.

From May 2023 to December 2024, a total of 209 UAV flights were conducted at the site, corresponding to approximately 100 h of cumulative flight time. After data quality controls, including the removal of records affected by rainfall and other conditions that could compromise instrument performance, results from 168 flights were retained for analysis. These included 40 flights in spring, 55 in summer, 53 in autumn, and 20 in winter, defined according to the Northern Hemispheric seasons.

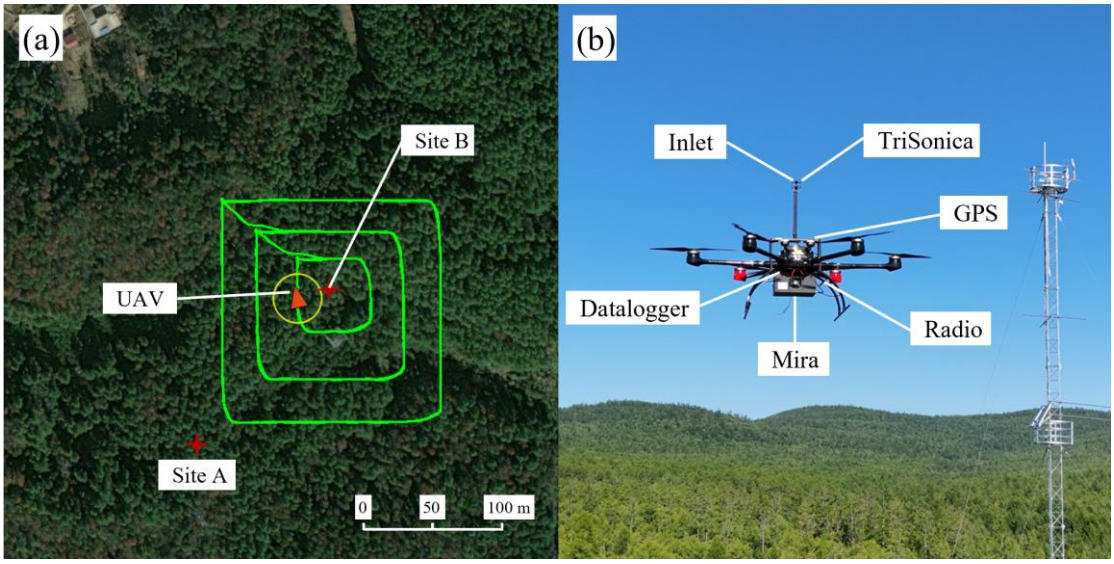



**Figure 2.** (a) A top-down view of the UAV's flight tracks from a representative flight. The green flight tracks represent the box pattern, categorized into three box sizes: 50×50×50 $m^3$, 100×100×50 $m^3$, and 150×150×50 $m^3$. Site A marks the location of the flux tower where EC measurements of vertical $CO_2$ fluxes are continuously carried out, while Site B denotes the take-off point for the profile pattern. The straight-line distance between the two sites is 150 m. All UAV flights were conducted following the same predefined flight routes. (b) The instrumented UAV platform; the flux tower can be seen in the background.

## 2.3 Flight patterns

Two complementary flight strategies were executed in this study: a box pattern and a profile pattern (Fig. 3a). The box pattern consists of a closed rectangular flight path flown above the forest canopy at multiple altitudes, enabling sampling of horizontal $CO_2$ transport across a defined control volume. Box flights were conducted at heights of 35, 40, 45, 50, 60, and 85 m above ground level. Using flight-path fitting and screen interpolation, the three-dimensional spatial distributions of $CO_2$ volume

mixing ratio, wind vectors, and air density were reconstructed within the box domain. In the present study, we reconstructed the spatial distributed data for visualization purposes only (Fig. 3b), but computed the horizontal fluxes using the original observations directly. Flight-path fitting refers to the construction of a smooth, closed loop constructed from the discrete UAV trajectories at all altitudes, thereby defining the four virtual vertical surfaces of the box. Screen interpolation refers to the mapping of $CO_2$ mixing ratios and corrected wind speed measurements observed along the flight path onto a regular two-dimensional grid on the vertical surfaces for visualization of spatial patterns.

The profile pattern was designed to capture vertical gradients of $CO_2$ mixing ratios, wind speed, and air density from near the surface to the top measurement height. Each box-pattern flight was paired with a vertical profile, and all measurements were completed within approximately 20 min to ensure consistency of the sampled air mass in the controlled volume. Vertical $CO_2$ fluxes were computed from the profile data using the gradient method (Sect. 3.2.2), with the analysis height range defined by the lowest and highest box levels (35-85 m). Because the EC system is installed at 31 m, UAV-derived $CO_2$ vertical fluxes used data from 26 and 36 m to enable direct comparison with tower-based EC measurements.

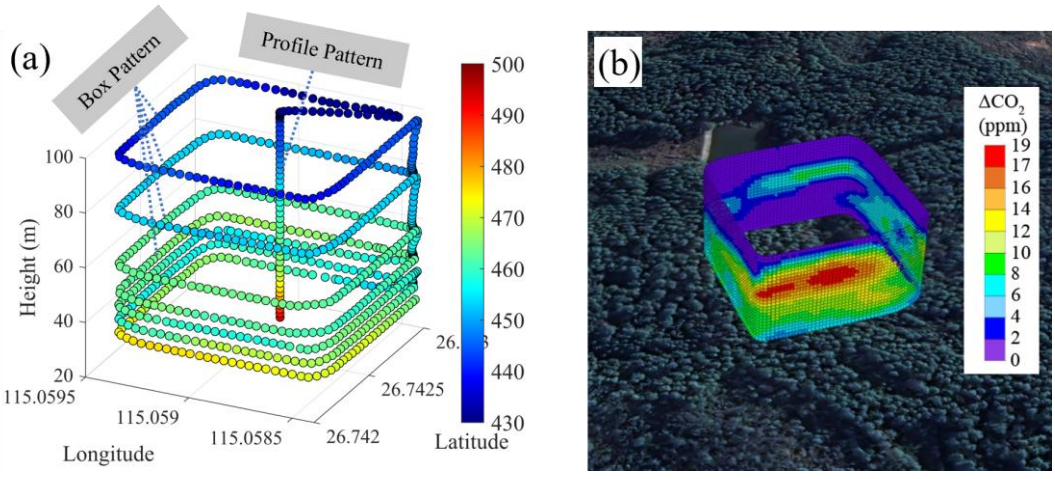



**Figure 3.** Overview of flight patterns. (a) Two distinct flight strategies: box pattern and the profile pattern. (b) The spatial distribution of $CO_2$ mixing ratios obtained through flight-path fitting and screen interpolation for flights during 2024-08-08 7:00 - 7:30, morning.

# 3 Methodologies

## 3.1 Wind speed calibration

To obtain accurate and reliable wind speed measurements, the raw data acquired by the ultrasonic anemometer were processed using a dedicated wind speed calibration algorithm. This algorithm, developed by Yang et al. (2025), was specifically developed for the UAV platform and the mounted instrumentation used in this study, and employs computational fluid dynamics (CFD) simulations to characterize the flow-field distortion by the UAV rotor-induced airflows. Hundreds of simulation scenarios were conducted, encompassing a wide range of flight altitudes, wind directions, and ambient wind speeds, in order to quantify the influence of rotor-induced airflow disturbances on wind measurements. The simulated disturbance fields were subsequently combined with UAV motion and attitude compensation schemes, yielding a comprehensive correction algorithm that simultaneously accounts for UAV translation, rotation, and rotor effects. The algorithm was validated with 3-D wind measurements at multiple levels on an 80-meter met tower Yang et al. (2025). All wind measurements used in this study were corrected using this algorithm, ensuring consistency and comparability with reference-grade wind observations.

## 3.2 $CO_2$ emission estimation based on UAV measurements

$CO_2$ emissions from within the control volume defined by the virtual box were quantified using a mass-balance framework that integrates measurements obtained from box-pattern and profile-pattern UAV flights. This approach assumes that $CO_2$ emitted within the control volume is transported by the mean wind field and becomes sufficiently mixed, such that the net emission rate can be inferred from the fluxes crossing the boundaries of the volume. Under steady or quasi-steady wind conditions, the mass flux of a chemical compound through a plane perpendicular to the mean wind direction can be considered approximately constant.

According to the divergence theorem, the rate of change of mass of a stable compound within a control volume equals the surface integral of the mass flux through

its enclosing surfaces. Consequently, the total $CO_2$ emission rate within the volume equals the net outward flux integrated across all box wall surfaces, where positive flux contributions represent $CO_2$ mass leaving the box and negative flux contributions represent $CO_2$ mass entering the box. Based on the integral form of the continuity equation, the emission rate within the control volume enclosed by the box pattern can be expressed as

$$E_C = E_{C,H} + E_{C,HT} + E_{C,V} + E_{C,VT} - E_{C,M} \quad (3.1)$$

where $E_C$ denotes the total $CO_2$ emission rate within the control volume, $E_{C,H}$ and $E_{C,V}$ denote the integrals of horizontal and vertical advective fluxes through the box walls, respectively; $E_{C,HT}$ and $E_{C,VT}$ represent the integrated turbulent fluxes in the horizontal and vertical directions, and $E_{C,M}$ accounts for changes in $CO_2$ mass associated with air-density variations. Eq. (3.1) forms the basis of the TERRA emission inversion model (Gordon et al., 2015).

To investigate the contributions of each component to the emissions, the TERRA model was updated here, in particular the treatment of the vertical flux algorithm, to directly compute vertical turbulent fluxes based on the UAV measurements instead of relying on parametrization assuming entrainment. Here, the mean wind vectors ($\bar{u}$, $\bar{v}$, $\bar{w}$) measured with the UAV sonic anemometer over a 30-minute period and the corresponding wind fluctuations ($u'$, $v'$, $w'$), obtained by subtracting the 30-minute mean wind components from the instantaneous wind measurements, are used to determine fluxes in the three directions. For the horizontal terms, the mean horizontal wind speed $\bar{u}$ can be regarded as the main contributor to the $E_{C,H}$ term, typically 2-3 m/s. The horizontal turbulent velocity ($u'$) is the main contributor to $E_{C,HT}$. Using the 95th percentile of $u'$, the turbulent velocity is less than 0.1 m/s. The horizontal advection term ($E_{C,H}$) is larger than the turbulence term ($E_{C,HT}$) by more than a factor of 20, so that the $E_{C,HT}$ term can be neglected from Eq. (3.1). For the vertical flux terms, the reverse is true; the mean vertical wind speed $\bar{w}$, at typically <0.02 m/s, makes $E_{C,V}$ a minute contribution compared to the turbulent flow contribution $E_{C,VT}$, which depends on the vertical turbulent velocity ($w'$). Using the 95th percentile of $w'$, the turbulent velocity can reach 0.3 m/s. As such, vertical advection term can also be

neglected from Eq. (3.1).

The density-related term can be expressed as

$$E_{C,M} = M_R \iiint \chi_C \frac{d\rho_{air}}{dt} dxdydz \quad (3.2)$$

Because the maximum vertical (≈50 m), horizontal (≈150 m) extents, and duration of the UAV flights are limited, air-density variation over time $\frac{d\rho_{air}}{dt}$ within the control volume can be assumed to be negligible, and $E_{C,M}$ was therefore neglected. Accurate estimation of the remaining flux terms ($E_{C,H}$ and $E_{C,VT}$) enables computation of the net $CO_2$ emission rate. The reliability of the box-pattern approach for resolving $CO_2$ emission is further supported by Han et al. (2024), who conducted a series of controlled UAV-based $CO_2$ validation experiments over an industrial coking facility.

### 3.2.1 Computation of $CO_2$ horizontal emission component

The horizontal emission component was derived from box-pattern measurements by integrating the advective $CO_2$ flux across the four vertical walls of the virtual box. The horizontal $CO_2$ emission rate can be written as

$$E_{C,H} = M_R \oiint \chi_C(s,z)\rho_{air}(s,z)u_n(s,z)dsdz \quad (3.3)$$

where $E_{C,H}$ is the horizontal $CO_2$ emission, $M_R$ is the ratio of the molar mass of $CO_2$ to that of air, $\chi_C(s,z)$ is the $CO_2$ mole fraction, $\rho_{\mathrm{air}}(s,z)$ is the air density, and $u_n(s,z)$ is the wind speed component normal to the flight path at point $(s,z)$. Here, $z$ denotes the flight altitude, $s$ represents the path position along the flight trajectory starting from a predefined fix position on the trajectory path, and $(s,z)$ indicates the point located at the path position $s$ at flight altitude $z$.

For each altitude level $z_i$, the line flux $F(z_i)$ was first calculated from the box-pattern data as

$$F(z_i) = M_R \sum_{j=1}^{N_i} \chi_C(s_j,z_i) \cdot \rho_{air}(s_j,z_i) \cdot u_n(s_j,z_i) \cdot \Delta s_j \quad (3.4)$$

where $j$ denotes the sampling point index along the flight path at altitude $z_i$, $N_i$ is the total number of sampling points at altitude $z_i$, and $\Delta s_j$ is the flight distance

represented by the $j$-th sample interval.

To suppress small-scale variability, a moving average was applied to consecutive line-flux values, yielding layer-averaged fluxes for discrete altitude intervals. These values were then vertically integrated to obtain the total horizontal $CO_2$ emission rate

$$E_{C,H} = \sum_{i=1}^{n} F(z_i)\Delta z_i = M_R \sum_{i=1}^{n} \left( \sum_{j=1}^{N_i} \chi_C (s_j, z_i) \rho_{\text{air}}(s_j, z_i) u_n(s_j, z_i) \Delta s_j \right) \Delta z_i \tag{3.5}$$

where $i$ denotes the vertical layer index from the first layer to the $n$-th layer, $n$ is the total number of vertical layers, and $\Delta z_i$ is the thickness of the $i$-th altitude interval. In this study, the first observed altitude layer $z_1$ corresponds to the lowest UAV sampling height (35 m above ground level).

### 3.2.2 Computation of $CO_2$ vertical emission component

The vertical $CO_2$ emission component was estimated from profile measurements using the gradient method, which relates turbulent scalar fluxes to vertical gradients of the scalar concentration. In practice, vertical profiling over forested terrain is operationally challenging, and UAV measurements were conducted at a single representative location. The resulting vertical fluxes were assumed to be representative of the broader domain, an assumption evaluated through direct comparison with eddy covariance (EC) flux tower measurements (see Section 4.2.1).

The vertical $CO_2$ emission component was obtained from integrating the vertical flux over the horizontal area enclosed by the box pattern and can be approximated by the product of vertical flux and the horizontal area, expressed as

$$E_{C,VT} = \iint F_v dx dy = A \cdot F_v \tag{3.6}$$

where $F_v$ denotes the vertical flux and $A$ is the horizontal area of the control volume.

According to the flux-gradient relationship (Kaimal and Finnigan, 1994), turbulent scalar fluxes are proportional to the vertical gradient of the scalar quantity:

$$F_v = -\rho_{air} K_C \frac{\partial \bar{c}}{\partial z} \tag{3.7}$$

where $K_C$ denotes turbulent exchange coefficient, $\bar{c}$ was obtained by converting the measured $CO_2$ mixing ratio to concentration using the concurrently measured temperature and pressure during the UAV profile flight.

A mixing-length formulation was adopted, in which the eddy diffusivity is expressed as the product of a mixing length and a velocity scale represented here by the friction velocity (Lee and Mahrt, 2005)

$$K_M = l u_* \tag{3.8}$$

where $l$ is the mixing length and $K_M$ is the exchange coefficient for momentum. Under neutral stratification conditions, $K_C$ can be assumed to be equal to $K_M$, and the friction velocity is defined as

$$u_* = l\frac{\partial \bar{u}}{\partial z} = \kappa z \frac{\partial \bar{u}}{\partial z} \tag{3.9}$$

where $\kappa$ is the von Karman constant ($\kappa$=0.4), $\frac{\partial \bar{u}}{\partial z}$ is the vertical gradient of the mean wind speed.

To account for atmospheric stratification, a stability correction (Budyko et al., 1962) was introduced as

$$l = m\kappa z \tag{3.10}$$

where $m$ is the stratification correction parameter, determined as a function of the gradient Richardson number ($R_i$) according to Budyko's study

$$m = (1 - R_i)^{1/2} \tag{3.11}$$

Under neutral stratification conditions ($R_i = 0$), m = 1. For computational convenience, the gradient Richardson number $R_i$ is approximated by the bulk Richardson number $R_B$ in finite-difference form

$$R_i \approx R_B = \frac{\frac{g\Delta\bar{\theta}}{\bar{\theta}\Delta z}}{\left(\frac{\Delta\bar{u}}{\Delta z}\right)^2} = \frac{g}{\overline{\theta_1}+\overline{\theta_2}} \frac{(\overline{\theta_2}-\overline{\theta_1})(z_2-z_1)}{(\overline{u_2}-\overline{u_1})^2} \tag{3.12}$$

where $g$ is the gravitational acceleration constant; $\Delta\bar{\theta}$ and $\Delta\bar{u}$ represent the changes in the temperature and wind speed between the layers ($\Delta z$), after smoothing with a seven-point moving window. In applying Eq. (3.12), the smoothed $\bar{\theta}$ and $\bar{u}$ vertical profiles are directly used to compute $R_B$, taking respective data points from two adjacent heights, $z_1$and $z_2$, using the smoothed temperature and wind speed profiles

at the two heights for $\overline{u_1}$, $\overline{u_2}$, $\overline{\theta_1}$, and $\overline{\theta_2}$. When applying the gradient method to estimate the flux, the vertical separation, $\Delta z = z_2 - z_1$, is typically chosen within a range of 1-10 m (Meredith et al., 2014). In this study, $\overline{u_1}$, $\overline{u_2}$ and $\overline{\theta_1}$, $\overline{\theta_2}$ were taken 5 m below and 5 m above any target height ($\Delta z = 10$ m), respectively, during the UAV ascent in the vertical profile measurements.

Because forest canopies represent aerodynamically rough and structurally complex surfaces, wind profiles above the canopy may deviate from the ideal logarithmic form. Following the neutral logarithmic wind-profile formulation from Monin–Obukhov similarity theory (Raupach, 1994), the surface-layer mean wind profile ($\bar{u}$) was expressed as

$$\bar{u} = \frac{u_*}{\kappa} ln \frac{z-d}{z_0} \tag{3.13}$$

where $d$ is the zero-plane displacement height, which for this type of forest is typically taken as 70%-80% of the vegetation height, and $z_0$ is the surface roughness length.

Assuming neutral atmospheric stratification and treating $u_*$, $d$, and $z_0$ as constants over the same time period, $u_*$ can be derived from wind measurements at two heights thereby eliminating $z_0$ from Eq. (3.13) and rearranging the equation so that

$$u_* = \frac{\kappa(\overline{u_2}-\overline{u_1})}{\ln[(z_2-d)/(z_1-d)]} \tag{3.14}$$

Substituting Eq. (3.10), Eq. (3.11) and Eq. (3.14) into Eq. (3.8) yields

$$K_c = \kappa^2(1-R_i)^{1/2} \frac{(\overline{u_2}-\overline{u_1})}{\ln[(z_2-d)/(z_1-d)]}(z-d) \tag{3.15}$$

Further substituting Eq. (3.15) into Eq. (3.7) and integrating the latter result in the vertical flux

$$F_v = \rho_{air}\kappa^2(1-R_i)^{1/2} \frac{(\overline{u_2}-\overline{u_1})(\overline{c_1}-\overline{c_2})}{\{\ln[(z_2-d)/(z_1-d)]\}^2} \tag{3.16}$$

where $\overline{c_1}$ and $\overline{c_2}$ represent the mean concentrations of $CO_2$ at heights $z_1$ and $z_2$, respectively, converted from measured $CO_2$ mixing ratios at using the measured temperature and pressure at both heights. In this study, $z_1$ and $z_2$ correspond to 5 m below and 5 m above the target height, respectively, during the UAV ascent.

The vertical $CO_2$ emission ($E_{C,VT}$) is finally expressed as

$$E_{C,VT} = A\rho_{air}\kappa^2(1-R_i)^{1/2}\frac{(\overline{u_2}-\overline{u_1})(\overline{c_1}-\overline{c_2})}{\{\ln[(z_2-d)/(z_1-d)]\}^2} \quad (3.17)$$

In summary, horizontal $CO_2$ emission components were derived from box-pattern measurements using the divergence theorem, whereas vertical emission components were obtained from profile-pattern measurements using the gradient method. Finally, the three-dimensional net $CO_2$ emission was obtained using the original observations. The reliability of the vertical flux estimates, computed using Eq (3.16), was evaluated through direct comparisons with results from flux tower observations (see Section 4.2.1).

## 3.3 Stationary tower-based data processing

The EC system installed at the flux tower consists of a three-dimensional ultrasonic anemometer (CSAT3, Campbell Scientific, USA), an open-path $CO_2$/$H_2O$ analyzer (LI-7500, LI-COR Biosciences, USA), and a datalogger (CR3000, Campbell Scientific, USA). Raw data are acquired at a sampling frequency of 10 Hz. In the present study, concurrent EC data from tower were processed during which the time lag between wind and gas measurements was corrected following the method of Sahlée et al. (2007), and standard quality-control procedures were applied to the turbulence data (*SI Appendix*, S1).

Fluxes were computed over 30 min averaging intervals, and coordinate rotation, virtual temperature correction, and frequency-response correction were applied to ensure high-quality vertical flux estimates. Following standard eddy covariance formulations (Webb et al., 1980; Baldocchi, 2003), the friction velocity ($u_*$) and scalar fluxes ($F_v$) were computed as

$$u_* = (-\overline{u'w'})^{1/2} \quad (3.18)$$

$$F_v = \rho_{air}\overline{w'c'} \quad (3.19)$$

where the primes denote turbulent fluctuations of the corresponding variables.

# 4 Results and discussion

## 4.1 Gas analyzer comparison test

To evaluate the consistency between different $CO_2$ analyzers, ground-based intercomparison experiments were conducted using an open-path $CO_2/H_2O$ gas analyzer (LI-7500), which was part of the eddy covariance system, and the closed-path analyzer (MIRA) used on the UAV. The experiment was performed from 21:00 to 22:00 local time on 12 August 2024 (Fig. 4). The air inlets of the two analyzers were positioned at the same height to ensure sampling of the same air mass, with the LI-7500 operating at 10 Hz and the MIRA analyzer at 1 Hz. A fixed time lag of 5 s, associated with air flow through the sampling line, was applied to synchronize the MIRA measurements with the LI-7500 data.

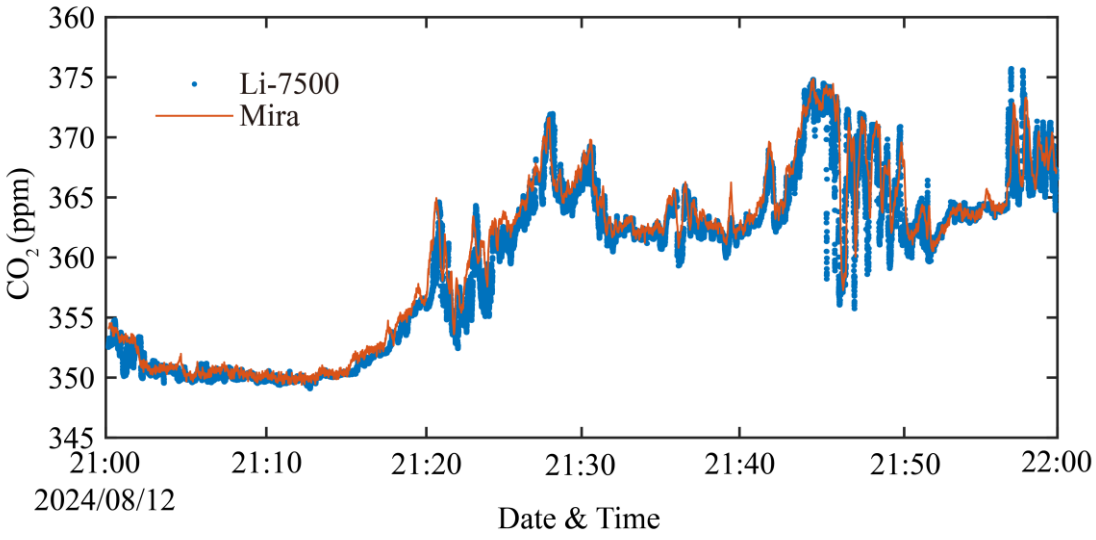



**Figure 4.** The comparative chart of $CO_2$ mixing ratio measured by the LI-7500 and Mira.

As shown in Fig. 4, the $CO_2$ mixing ratios measured by the two instruments exhibit highly consistent temporal variabilities, although small differences in absolute values and short-term fluctuations are present. Both datasets show a pronounced increase in $CO_2$ mixing ratio during the initial phase of the experiment, followed by enhanced variability with multiple peaks, and sustained elevated concentrations during the later

period. The overall temporal coherence between the two datasets is strong, indicating that both instruments capture the same underlying $CO_2$ fluctuation dynamics. The MIRA measurements tend to report slightly lower $CO_2$ mixing ratios than the LI-7500. This attenuation is primarily attributed to high-frequency losses associated with the closed-path sampling system, including viscous damping and signal smoothing during sample transport through the 1/8-inch outer-diameter polytetrafluoroethylene (PTFE) sampling tube. Because the sampling tube used in this study was relatively short (approximately 0.5 m) and the sample residence time inside the tube was 0.5 s, its influence on $CO_2$ measurements is expected to be limited. Such attenuation is a well-documented characteristic of closed-path systems and does not compromise the ability of the analyzer to resolve mean concentration levels and mesoscale variability (Burba et al., 2012; Metzger et al., 2016). In summary, despite minor attenuations at high frequencies, the closed-path MIRA analyzer demonstrates a strong agreement with the EC-based LI-7500 measurements, supporting its suitability for $CO_2$ measurements from the UAV-based platform.

Further, the scatterplot of the $CO_2$ measurement results from both instruments, shown in Fig. 5, reveals a strong linear relationship. The data are closely distributed around a narrow band of the fitted linear regression line, with a correlation coefficient of $r$ = 0.986. Because both analyzers are subject to measurement uncertainties, reduced major axis (RMA) regression was applied. The RMA regression yielded a slope of 1.19 and an intercept of 0.64 ppm. The close clustering of the data points around the fitted line indicates low random error and high precision between the two instruments. This regression result indicates that the UAV observations were able to capture temporal variability in $CO_2$ in the real atmosphere, such as minute-scale increases, decreases, and multi-peak structures. In addition, the calculations of the horizontal line flux divergence and the vertical flux both require subtraction of the background $CO_2$ concentration and estimation of the $CO_2$ gradient, respectively. Therefore, the systematic bias between the two instruments is expected to have a negligible impact on the flux calculations.

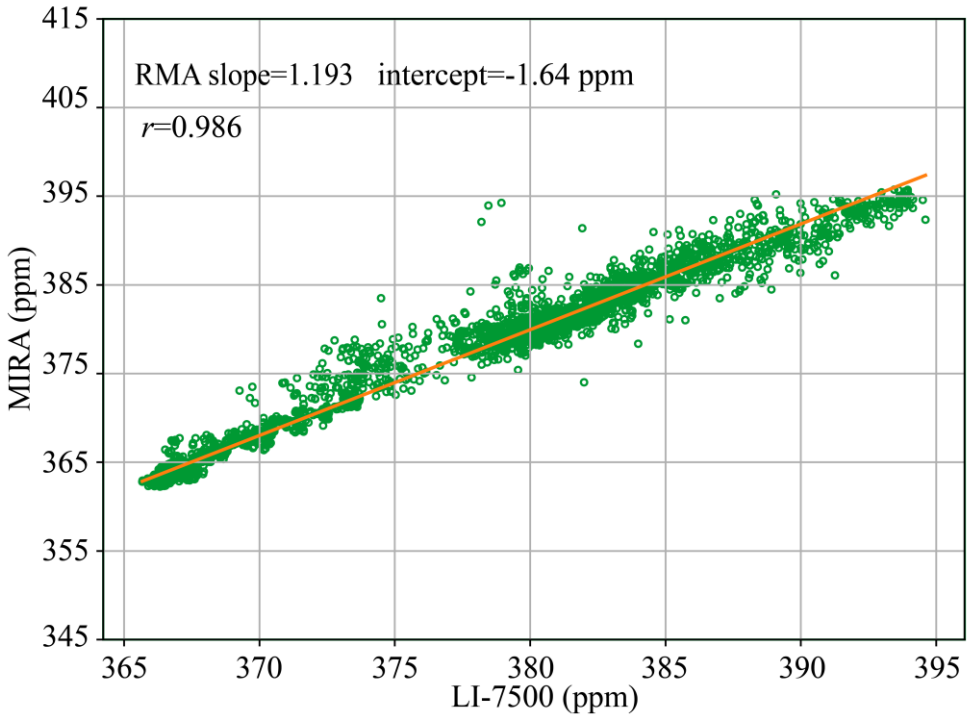



**Figure 5.** Scatterplot comparison of $CO_2$ mole fractions measured by the UAV-mounted MIRA analyzer and the flux-tower LI-7500 analyzer. The orange line denotes the reduced major axis (RMA) regression. The regression yielded a slope of 1.193 and an intercept of -1.64 ppm, with a correlation coefficient of r = 0.986, indicating strong agreement between the two instruments under field conditions.

## 4.2 In-flight comparison test

### 4.2.1 Seasonal variability of vertical fluxes

A key part of the present study is to determine reliable vertical flux measurements using the UAV platform over a forest ecosystem on complex terrains. To quantitatively evaluate the agreement between UAV-based profile retrievals and flux tower measurements, the UAV-derived vertical $CO_2$ flux ($F_v$) and friction velocity ($u_*$) are compared against their EC counterparts (Fig. 6). Because both datasets contain measurement uncertainties, the Reduced Major Axis (RMA) regression (Smith, 2009; Warton et al., 2006) was used, which is more appropriate than ordinary least squares when neither datasets can be treated as error-free. The season-specific RMA slope, intercept, and Pearson correlation coefficient ($r$) are summarized in Table 3. For the comparison with the EC system installed at 31 m above ground, the UAV-derived

vertical flux was calculated using measurements at $z_2$=26 m and $z_1$=36 m.

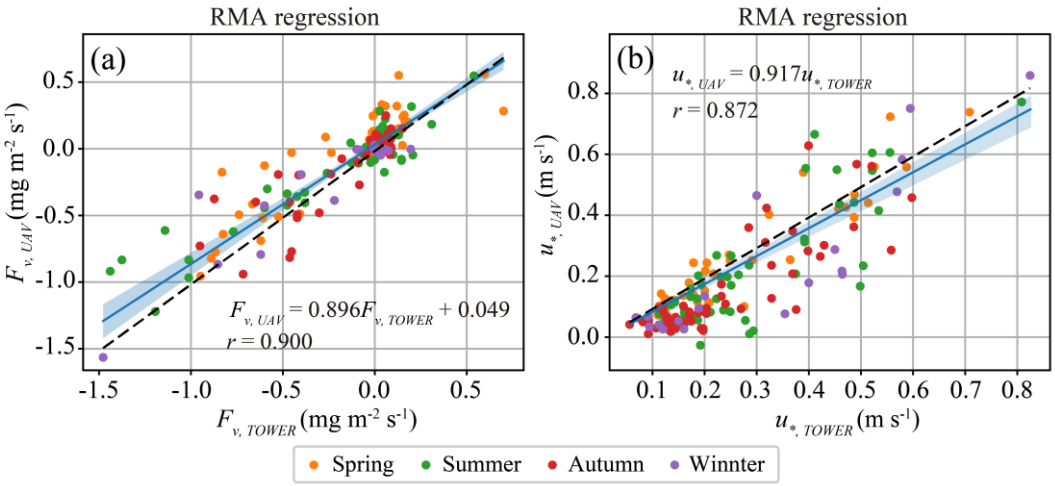



**Figure 6.** Reduced major axis (RMA) regressions comparing UAV-based measurements with flux tower observations across all seasons. Panel (a) shows $CO_2$ flux ($F_v$) and panel (b) shows friction velocity ($u_*$). In both panels, the x axis represents the flux tower measurements and the y axis represents the UAV-based measurements. Points are colored by season (Spring, Summer, Autumn, Winter). The solid blue line denotes the RMA fit, the shaded band indicates the 95% confidence interval (CI) of the regression line, and the dashed black line represents the 1:1 reference. The regression equations are expressed using the corresponding physical variables in each panel, and the Pearson correlation coefficient ($r$) is also reported.

**Table 3.** Seasonal reduced major axis (RMA) regression results comparing UAV-derived measurements with flux tower observations for $CO_2$ flux ($F_v$) and friction velocity ($u_*$). Seasons are defined according to the three-month meteorological seasons: spring (March-May), summer (June-August), autumn (September-November), and winter (December-February). For each season, the table reports the sample size ($n$), correlation coefficient ($r$), RMA slope and its 95% confidence interval (CI), and the intercept. The $u_*$ regressions are constrained to pass through the origin (intercept fixed at 0).

| Variables | Season | $n$ | $r$ | Slope | 95% CI of Slope | Intercept |
|---|---|---|---|---|---|---|
| $F_v$ | Spring | 40 | 0.890 | 0.928 | [0.777, 1.074] | 0.127 |
| | Summer | 52 | 0.938 | 0.801 | [0.694, 0.929] | 0.034 |
| | Autumn | 55 | 0.863 | 0.997 | [0.771, 1.281] | 0.022 |
| | Winter | 20 | 0.917 | 0.940 | [0.551, 1.079] | 0.013 |
| $u_*$ | Spring | 40 | 0.942 | 1.012 | [0.926, 1.093] | 0 |
| | Summer | 52 | 0.845 | 0.915 | [0.790, 1.021] | 0 |

| | | | | | |
|---|---|---|---|---|---|
| Autumn | 55 | 0.843 | 0.819 | [0.679, 0.951] | 0 |
| Winter | 20 | 0.884 | 0.914 | [0.677, 1.059] | 0 |

As shown in Fig. 6a, UAV-derived $F_{v,UAV}$ exhibits a clear linear relationship with EC $F_{v,TOWER}$, with points generally distributed around the 1:1 line, indicating that the UAV approach captures the temporal variability of canopy-scale vertical $CO_2$ exchange. Table 3 further demonstrates consistently strong coefficients of determination across seasons ($r$=0.863-0.938). The slope, slightly lower than unity, suggests a modest "range compression" in the UAV-derived fluxes, meaning that the magnitudes tend to be slightly attenuated under strong emission or strong uptake conditions (large positive/negative fluxes). In spring, the slope is 0.928 (95% CI: [0.777, 1.074], $r$=0.890), and in autumn the slope is 0.997 (95% CI: [0.771, 1.281], $r$=0.863); both are close to unity and their confidence intervals encompass 1, suggesting good consistency in flux magnitude. In summer, the slope decreases to 0.801 (95% CI: [0.694, 0.929], $r$=0.938), and the confidence interval does not include 1, indicating a smaller flux magnitude during periods of stronger exchange. Hence the slightly lower $F_{v,UAV}$ than $F_{v,Tower}$ likely reflects enhanced nonstationarity and rapid scalar fluctuations during peak growing season, which increase sensitivity to sampling height from ground and platform-related perturbations. In winter, the slope is 0.940 (95% CI: [0.551, 1.079], $r$=0.917), showing strong correlation but larger uncertainty due to the smaller sample size (n=20).

Figure 6b shows a clear linear relationship between friction velocity $u_{*,UAV}$ and $u_{*,TOWER}$. Because $u_*$ should physically approach zero under very weak turbulence, an origin-constrained regression (intercept fixed at 0) was used to avoid non-physical extrapolation from a free intercept. The full-sample RMA regression is:

$$u_{*,UAV}=0.917(\pm0.063)u_{*,TOWER},\ r=0.872 \quad (4.1)$$

This result indicates that the UAV platform captures the variations in turbulent intensity well ($r$=0.872), while the slope below unity suggests a slight multiplicative underestimation of $u_*$ relative to tower observations. Regressions for different seasons

(Table 3) further indicate that the best agreement occurs in spring, with a slope of 1.012 (95% CI: [0.926, 1.093], $r$=0.942). In contrast, $u_{*,UAV}$ shows a slight underestimation relative to $u_{*,TOWER}$ in summer, autumn, and winter, respectively, with a slope of 0.915, 0.819, 0.914.

Taken together, Fig. 6 and Table 3 demonstrate that the fluxes and turbulence metrics derived from the UAV measurements reproduce well the tower-observed variability of both canopy-scale $CO_2$ exchange and key turbulence characteristics across all seasons ($r$=0.900 for $F_v$ and $r$=0.872 for $u_*$), supporting the feasibility and robustness of such UAV profile measurements for monitoring above-canopy exchange. Nevertheless, two systematic features warrant attention: (i) $F_v$ magnitudes tend to be slightly underestimated in summer (slope significantly < 1), and (ii) $u_*$ shows a slight overall underestimation under the origin-constrained regression.

### 4.2.2 Diurnal variability of vertical fluxes

To further evaluate the applicability and consistency of the UAV-based profiling method under different diurnal conditions, the UAV-derived $F_v$ estimates were grouped and compared with results from EC observations in three time periods: early morning (06:00-08:00 LST), noon (13:00-15:00 LST), and evening (19:00-21:00 LST). Reduced Major Axis (RMA) regression was applied to both the vertical $CO_2$ flux ($F_v$) and the friction velocity ($u_*$) for each time period (Fig. 7), with the corresponding statistical results summarized in Table 4.

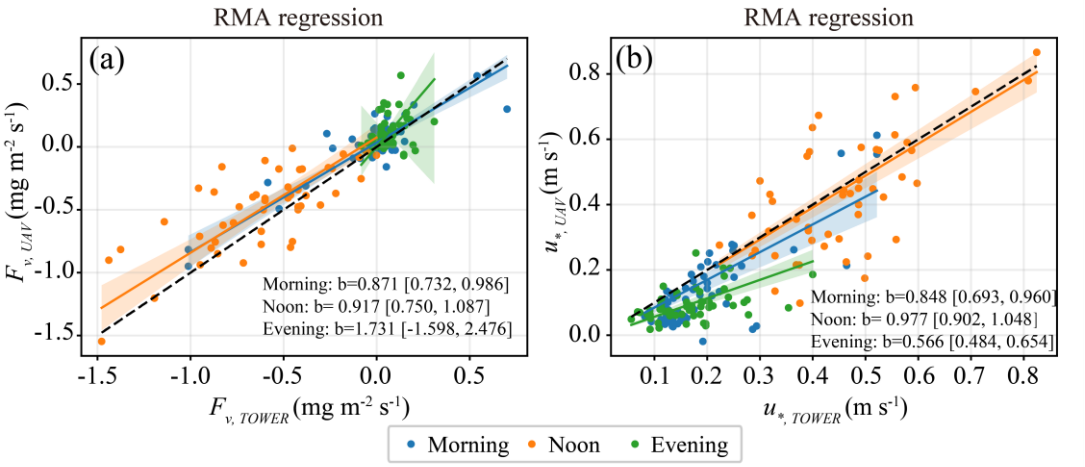



**Figure 7.** Reduced major axis (RMA) regressions comparing UAV-based measurements with flux tower observations for (a) $CO_2$ flux ($F_v$) and (b) friction velocity ($u_*$) grouped by time of day. In both panels, the x axis represents the flux tower measurements and the y axis represents the UAV-based measurements. Data are separated into morning (06:00-08:00 LST), noon (13:00-15:00 LST), and evening (19:00-21:00 LST) and shown with different colors. Solid colored lines represent the RMA fits for each time period, and the shaded bands indicate the 95% confidence intervals. The dashed black line denotes the 1:1 reference. Reported in each panel are the RMA slopes and their 95% confidence intervals; the $u_*$ regressions in panel (b) are constrained to pass through the origin (intercept fixed at 0).

As shown in Table 4, the RMA regressions for $F_v$ exhibit relatively strong correlations during the early morning and midday periods ($r$=0.898, $n$=63 and $r$=0.867, $n$=55, respectively). The corresponding slopes are 0.871 (95% CI: [0.732, 0.986]) for early morning and 0.916 (95% CI: [0.750, 1.087]) for midday, both close to unity but slightly lower than 1, indicating a modest amplitude compression. This suggests that the UAV-based method is generally capable of reproducing the variability of $CO_2$ fluxes observed by the EC system, while tending to underestimate flux magnitudes under stronger exchange conditions. This behavior is consistent with the seasonal-scale results presented in Section 4.2.1 and likely reflects the increased sensitivity of the gradient method to strong flux events under limited vertical sampling resolution and short-term nonstationary conditions.

**Table 4.** Reduced major axis (RMA) regression statistics for comparisons between UAV-based measurements and flux tower observations, grouped by time of day (morning, noon, and evening). Results are reported for $CO_2$ flux ($F_v$) and friction velocity ($u_*$), including sample size ($n$),

correlation coefficient ($r$), RMA slope, the 95% confidence interval (CI) of the slope, and the intercept. For $u_*$, the regression is constrained to pass through the origin (intercept fixed at 0).

| Variables | Period | $n$ | $r$ | Slope | Slope of 95% CI | Intercept |
|---|---|---|---|---|---|---|
| $F_v$ | Morning | 63 | 0.898 | 0.871 | [0.732, 0.986] | 0.034 |
| | Noon | 50 | 0.867 | 0.916 | [0.750, 1.087] | 0.075 |
| | Evening | 54 | 0.235 | 1.730 | [-1.598, 2.476] | 0.002 |
| $u*$ | Morning | 63 | 0.887 | 0.848 | [0.926, 1.093] | 0 |
| | Noon | 50 | 0.865 | 0.977 | [0.790, 1.021] | 0 |
| | Evening | 54 | 0.424 | 0.566 | [0.679, 0.951] | 0 |

In contrast, the agreement for $F_v$ deteriorates substantially during the evening period, with a low correlation coefficient ($r$=0.235, $n$=54) and a highly uncertain slope (1.730, with a 95% confidence interval spanning both positive and negative values). The possible reason for such a comparison result is that, under low evening turbulence, both the UAV-based and EC-based flux measurements become less reliable, because the vertical turbulent exchange weakens and the relative influence of non-turbulent transport terms increases. Under such conditions, the UAV methodology is subject to larger uncertainties in the derived vertical fluxes and shows an apparent low bias relative to the EC measurements. It should be noted, however, that EC vertical flux measurements under such low turbulence conditions also bear large uncertainties, and hence this comparison only implies a low bias in the UAV methodology relative to the EC methodology, and does not indicate the absolute errors in the UAV-determined $F_v$ nor that from the EC methodology. The diurnal variation of friction velocity ($u_*$) derived from the tower system (Fig. S1) shows a clear asymmetry between morning and evening transitions, with turbulence developing gradually after sunrise but decaying rapidly in the evening, which helps explain the poorer agreement under evening conditions. Furthermore, an analysis of the evening flux differences indicates that both UAV- and tower-derived vertical $CO_2$ fluxes are associated with greater uncertainties at evening, whereas the overall differences remain small and show no significant seasonal variations. A more detailed analysis of the evening flux differences

is provided in the *SI Appendix* S3.

Figure 8 illustrates the seasonal and diurnal variability of the UAV-derived vertical $CO_2$ fluxes across morning, noon, and evening periods for all four seasons. Distinct diurnal patterns are evident in every season. Midday periods consistently exhibit the strongest downward $CO_2$ fluxes, corresponding to maximum ecosystem uptake, particularly in spring, summer, and autumn. In contrast, morning and evening fluxes were much reduced from mid-day peaks, probably resulting from neutral or weakly positive turbulent mixing as well as from combined effect of weaker uptake/emissions of $CO_2$ under lower photosynthetic/respirational activities. This diurnal structure aligns with the canonical coupling between solar radiation, canopy photosynthesis, and boundary-layer turbulence.

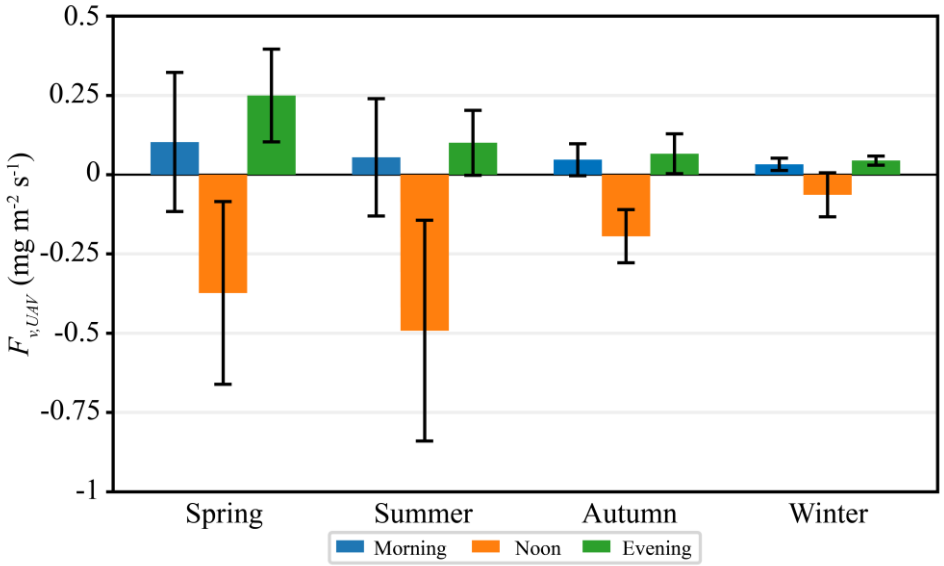



**Figure 8.** Seasonal variations of UAV-derived vertical $CO_2$ fluxes during morning, noon, and evening across spring, summer, autumn, and winter. Bars represent the mean flux for each period, and error bars indicate one standard deviation. Positive values denote upward (emission) fluxes, while negative values represent downward (uptake) fluxes.

Seasonal contrasts are equally pronounced. Summer and spring display the strongest net $CO_2$ uptake, consistent with favorable moisture conditions and strong radiative forcing in this subtropical forest. Autumn fluxes are weaker, reflecting declining physiological activity, while winter fluxes cluster near zero, with negligible

uptake or slight emissions across all periods. The ordering of seasonal uptake strength - summer > spring > autumn ≫ winter - is consistent with long-term EC observations at this site (Yu et al., 2008).

The observed diurnal and seasonal structures in the UAV-based vertical fluxes closely match those reported in previous tower-based studies at the Qianyanzhou station (Yu et al., 2006; Zhang et al., 2014) and in other temperate and subtropical forest ecosystems (Baldocchi, 2008; Goulden et al., 1996). These results therefore not only summarize the observed variability but also provide an ecologically meaningful consistency check for the UAV-based vertical flux approach.

## 4.3 UAV measurement results

Figure 9 provides a three-dimensional visualization of the $CO_2$ mole fraction anomaly field ($\Delta CO_2$), calculated relative to a constant background value defined as the mean of the lowest 5% of the time-series $CO_2$ observations, along the walls of the 100×100×50 $m^3$ control volume during the morning flight on 8 August 2024. The reconstructed $\Delta CO_2$ distribution exhibits pronounced spatial heterogeneity, with localized high-concentration patches embedded within relatively low-background regions. In particular, a distinct hotspot reaching ~40 ppm is observed near the upper-right sector of the box, while elevated $\Delta CO_2$ values also form elongated bands along portions of the lateral walls. This non-uniform pattern indicates that the near-canopy $CO_2$ field was far from horizontally homogeneous during the sampling window, consistent with the expectation of enhanced stratification and limited mixing in early morning conditions.

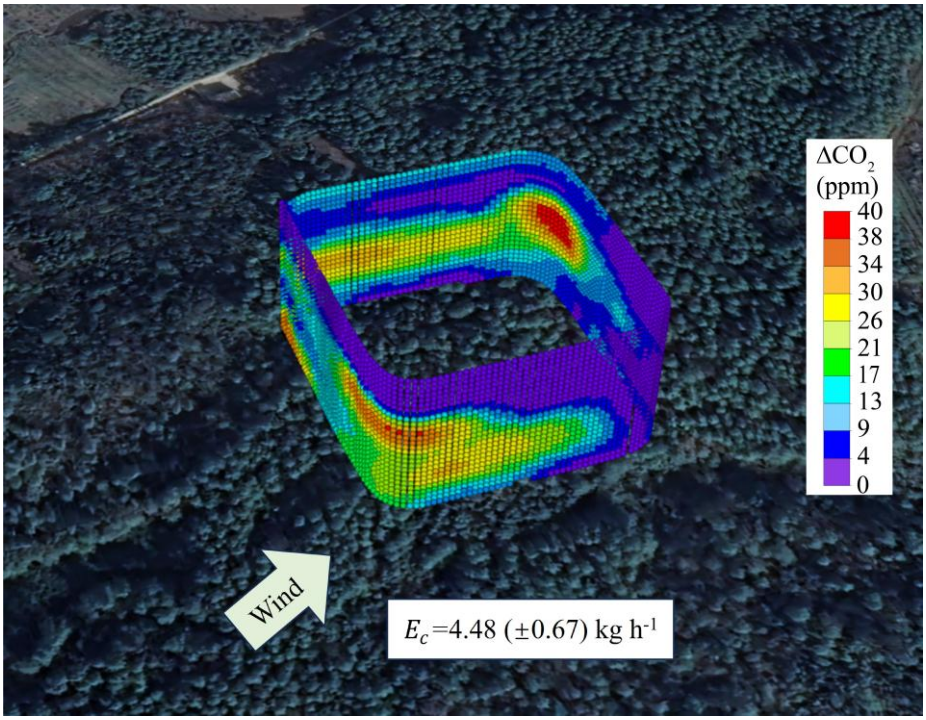



**Figure 9.** Three-dimensional distribution of the $CO_2$ mole fraction anomaly field ($\Delta CO_2$), obtained from processed and interpolated UAV measurements following the procedure described in Section 2.3, within the 100×100×50 $m^3$ domain during the morning flight on 8 August 2024, relative to a constant background value.

The wind vector shown in Fig. 9 indicates a prevailing southwesterly flow. The spatial alignment of the $\Delta CO_2$ enhancements with the box boundaries suggests that lateral advection and flux divergence played a central role in shaping the observed concentration gradients: $CO_2$-enriched air masses are transported into the control volume on the upwind side and redistributed along the walls, producing strong cross-boundary gradients that dominate the mass balance. Consistent with this interpretation, the box-mass balance calculation yields a positive net exchange rate of $E_c$ =4.48±0.67 kg $h^{-1}$ for the 100×100×50 $m^3$ control volume. Breaking down the individual mass balance terms indicates that the horizontal component ($E_{C,H}$ = 4.22±0.63 kg $h^{-1}$) accounts for nearly all of the net emission in the control volume, whereas the vertical component is small ($E_{C,VT}$ =0.26±0.04 kg $h^{-1}$). The near-zero vertical term is also consistent with the concurrent eddy-covariance observations similarly indicating a negligible turbulent vertical $CO_2$ flux. Therefore, the positive $E_c$ primarily reflects net $CO_2$ inflow driven by horizontal transport (i.e., lateral convergence) rather than local

vertical emission from the canopy.

Overall, the three-dimensional $\Delta CO_2$ structure shown in Fig. 9 highlights that, at this moment, $CO_2$ exchange above the forest canopy was controlled predominantly by horizontal transport under heterogeneous concentration fields. This underscores the importance of resolving spatial gradients and lateral boundary fluxes-features that can be captured by UAV sampling but are not directly observable from a single-point flux tower measurement.

## 4.4 Spatial heterogeneity of net $CO_2$ emission

To verify whether net emissions ($E_C$) calculated using the mass-balance approach differ across spatial scales, emission computations were made for three box-shaped control volumes constructed from the UAV flight tracks, with horizontal dimensions of 50×50 $m^2$, 100×100 $m^2$, and 150×150 $m^2$, respectively, and a common vertical extent of 50 m. The vertical contribution term $E_{C,VT}$ and the horizontal transport contribution term $E_{C,H}$ within each control volume were separately computed as per the detailed outlines above. The net emissions were normalized by the areas of the boxes to give area-normalized emission intensity $e_C = E_C/A$, where $A$ denotes the bottom area of the box. To minimize the influence of different time periods and seasons on the statistics, and according to the analysis in Section 4.2, the UAV measurements of $CO_2$ emissions collected in summer noon and autumn morning, which show better agreement with the flux tower comparisons, were selected for the spatial heterogeneity analysis. To ensure the validity of the comparison, measurements from the three virtual control volumes must be obtained within 20 minutes of each other. Under such a requirement, data from seven days of observations were used for the spatial heterogeneity analysis. Further examination of the measurement conditions during these periods showed that, for the summer noon cases, observations were conducted between 13:00 and 14:00 under predominantly southeasterly winds, while the fluxes measured by the fixed tower varied by less than 8% during the comparison period. For the autumn morning cases, observations were conducted between 06:00 and 07:00 under predominantly southwesterly winds, while the fluxes measured by the fixed tower varied by less than

5%. Overall, the observational conditions were considered sufficiently similar to support further comparative analysis.

If the $CO_2$ source-sink distribution in this region were spatially uniform, then by mass conservation the area-normalized emission intensity would be equal, i.e., $e_C(150) \approx e_C(100) \approx e_C(50)$ would be true. The means for the three box scales (see boxes in Fig. 10) were -0.25, -0.30, and -0.24 mg $m^{-2}$ $s^{-1}$, respectively. This indicates a pronounced net $CO_2$ uptake (i.e., negative emissions) of the system as a whole during summer at noon, while the differences among spatial scales are clearly smaller than the 22% systematic uncertainty. This result may suggest relatively weak spatial heterogeneity during the summer noon period. Furthermore, one-way ANOVA shows the mean differences in $e_C$ among the three scales were not significant, with an ANOVA $F$-statistic of 0.349, indicating low between-group variance relative to within-group variance, and a $p$-value of 0.710, indicating that the observed differences could be readily explained by random variation rather than a true scale effect. Overall, under summer noon conditions, the area-normalized net exchange intensity is insensitive to the horizontal scales examined, and within-group variability dominates (Fig. 10).

In addition, during summer at noon, the median values of $E_{C,H}/E_{C,VT}$ in Table 5 remain very small (from -0.025 to -0.006), indicating that the net $CO_2$ budget is dominated by the vertical turbulent-exchange term. This conclusion is further supported by the absolute magnitudes of the two components: the median $E_{C,H}$ values range only from 0.0687 to 0.273 kg $h^{-1}$, whereas the corresponding median $E_{C,VT}$ values range from -13.6 to -2.77 kg $h^{-1}$. Under summer noon conditions, stronger turbulence and more efficient vertical mixing likely suppress the relative influence of horizontal $CO_2$ gradients, so that horizontal transport contributes only a minor fraction to the virtual control volume budget. Although the negative values of $E_{C,H}/E_{C,VT}$ indicate that the horizontal and vertical components often have opposite signs, the magnitude of $E_{C,H}$ remains much smaller than that of $E_{C,VT}$.

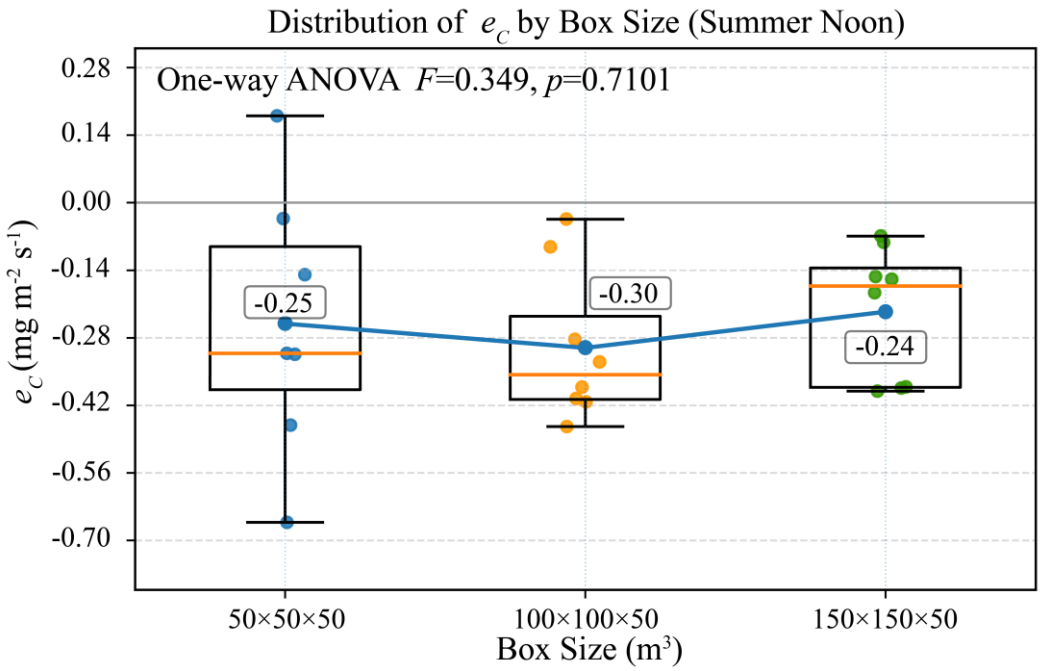



**Figure 10.** Distribution of $e_C$ across box sizes (50×50×50 m$^3$, 100×100×50 m$^3$, 150×150×50 m$^3$) of summer noon. Boxes represent the interquartile range (*IQR*), the center line is the median, and whiskers extend to 1.5×*IQR*. Colored points are individual samples. The blue solid polyline connects the mean $e_C$ of each group, with boxed numerical annotations. The reported $F$ and $p$ values denote the $F$-statistic and corresponding $p$-value from the one-way ANOVA, respectively.

**Table 5.** Summary statistics of net $CO_2$ emission estimates ($E_C$) derived from three box sizes during summer noon and autumn morning. For each box size, $n$ denotes the number of valid samples. Reported metrics include the mean and median of $E_C$ (kg h$^{-1}$), the interquartile range (*IQR*), the median and standard deviation (*SD*) of the horizontal-transport contribution ($E_{C,H}$) and the vertical-exchange contribution ($E_{C,VT}$), as well as the median ratio $E_{C,H}/E_{C,VT}$. All emission estimates are expressed in kg h$^{-1}$.

| | Summer Noon | | | Autumn Morning | | |
|---|---|---|---|---|---|---|
| Box Size (m$^3$) | 50×50×50 | 100×100×50 | 150×150×50 | 50×50×50 | 100×100×50 | 150×150×50 |
| $n$ | 7 | 7 | 7 | 7 | 7 | 7 |
| $E_C$ Mean (kg h$^{-1}$) | -2.24 | -10.6 | -18.6 | 0.166 | 7.64 | 9.35 |
| $E_C$ Median (kg h$^{-1}$) | -2.79 | -13.7 | -12.8 | 0.138 | 7.25 | 11.3 |
| *IQR* (kg h$^{-1}$) | 2.65 | 7.24 | 20.4 | 1.85 | 3.26 | 15.2 |
| $E_{C,H}$ Median (kg h$^{-1}$) | 0.0687 | 0.0817 | 0.273 | 0.105 | 3.52 | 6.41 |
| $E_{C,H}$ SD (kg h$^{-1}$) | 0.0162 | 0.0321 | 0.0732 | 0.0235 | 1.25 | 1.58 |
| $E_{C,VT}$ Mdian | -2.77 | -13.6 | -12.5 | 0.033 | 3.73 | 4.85 |

| | | | | | | |
|---|---|---|---|---|---|---|
| (kg $h^{-1}$) | | | | | | |
| $E_{C,VT}$ *SD* (kg $h^{-1}$) | 0.437 | 2.35 | 3.54 | 0.012 | 1.15 | 1.43 |
| Median $E_{C,H}/E_{C,VT}$ | -0.025 | -0.006 | -0.022 | 3.18 | 0.944 | 1.32 |

Another case study of spatial heterogeneity is based on the autumn morning dataset (Fig. 11). The mean values in Fig. 11 indicate that the emission intensities ($e_C$) derived for different box sizes (0.02, 0.21, and 0.11 mg $m^{-2}$ $s^{-1}$, respectively) differ to some extent. The differences among box sizes are substantially larger than the uncertainty of the method used in this study (15%), representing $e_C$ differ of various sizes. One-way ANOVA analysis also shows the differences in $e_C$ among the three scales were significant ($F$=4.482, $p$=0.025). This provides direct evidence that the net $CO_2$ emission intensity derived for the three virtual control volumes above the canopy is spatially heterogeneous.

In contrast, during autumn morning, the role of horizontal transport becomes much more pronounced. The median values of $E_{C,H}/E_{C,VT}$ increase to 3.18, 0.944, and 1.32 for the 50×50×50, 100×100×50, and 150×150×50 $m^3$ control volumes, respectively. Importantly, these elevated ratios reflect not only the presence of horizontal $CO_2$ gradients, but also the fact that the vertical turbulent-exchange component is comparatively weak during this period. Specifically, the median $E_{C,H}$ values range from 0.105 to 6.41 kg $h^{-1}$, while the median $E_{C,VT}$ values range from 0.033 to 4.85 kg $h^{-1}$. This indicates that, under weak-turbulence morning conditions, horizontal $CO_2$ transport can become comparable to, or even exceed, the vertical turbulent component. Such behavior is consistent with enhanced spatial heterogeneity in $CO_2$ exchange across the different control volumes. As the control-volume scale increases, small-scale horizontal gradient structures are progressively averaged out, reducing the relative contribution of $E_{C,H}$ and leading to the observed scale dependence of $E_C$. The component-wise contribution analysis (Table 5) indicates that the relative contribution of the horizontal transport term is markedly enhanced. The median metric, median $E_{C,H}/E_{C,VT}$, is 3.18 for 50×50×50 $m^3$, 0.944 for 100×100×50 $m^3$, and 1.32 for

847 150×150×50 $m^3$. These results suggest that there is a significant spatial heterogeneity
848 in the $CO_2$ emissions/uptake in the range covered by the different boxes leading to
849 horizontal $CO_2$ concentration gradients, and as a result near-surface horizontal $CO_2$
850 gradients under the measured horizontal winds are non-negligible within small control
851 volumes.

852 This scale sensitivity further highlights the true advantage of UAV observations
853 for characterizing spatial heterogeneity. UAV measurements can provide multipoint,
854 three-dimensional $CO_2$ distributions and associated wind speed gradient information
855 within a short time window, enabling the simultaneous estimation of $E_{C,H}$ (horizontal
856 transport) and $E_{C,VT}$ (vertical transport) within a consistent data framework. Moreover,
857 by varying the box sizes, the same dataset can be re-aggregated into different spatial
858 scales to facilitate a multi-scale comparison. In contrast, flux towers (eddy covariance)
859 essentially measure point-based vertical turbulent fluxes, whose representativeness is
860 determined by a footprint that varies with wind direction and atmospheric stability. As
861 a result, flux tower observations yield a footprint-weighted effective flux, making it
862 difficult to construct a spatial control volume and impossible to explicitly resolve the
863 lateral transport term $E_{C,H}$. Therefore, box-size dependence driven by spatial
864 heterogeneity is more readily captured by UAV observations, whereas flux towers are
865 limited in both observation geometry and the types of physical quantities they can
866 diagnose.
867

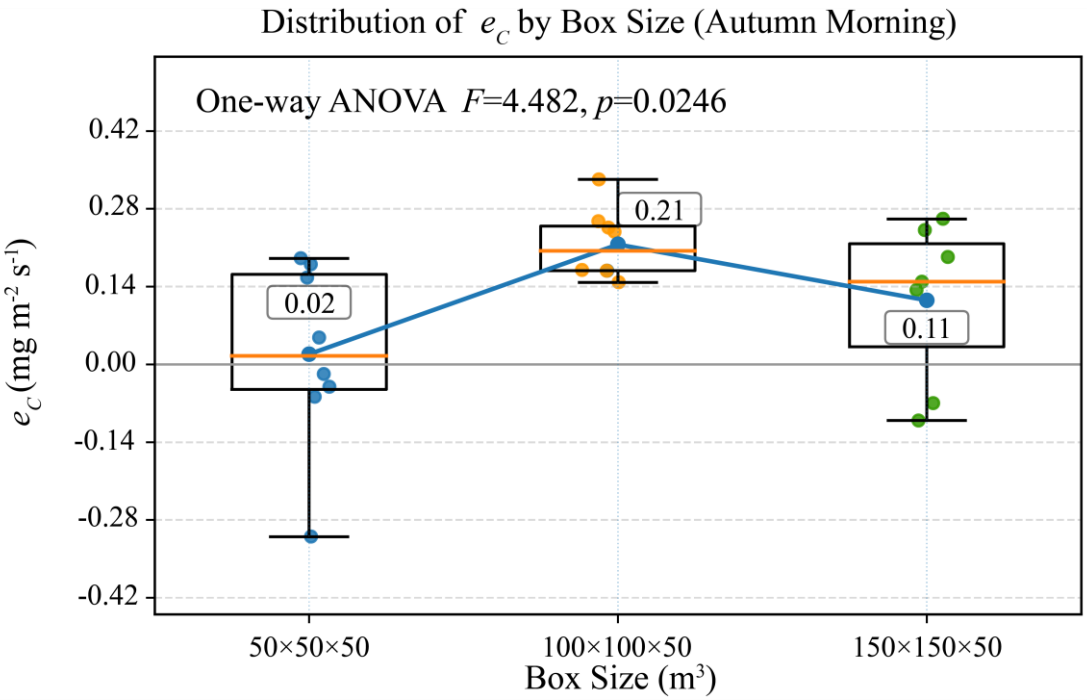



**Figure 11.** Distribution of $e_C$ across box sizes (50×50×50 m$^3$, 100×100×50 m$^3$, 150×150×50 m$^3$) of autumn morning. Boxes represent the interquartile range (*IQR*), the center line is the median, and whiskers extend to 1.5×*IQR*. Colored points are individual samples. The blue solid polyline connects the mean $e_C$ of each group, with boxed numerical annotations. The reported $F$ and $p$ values denote the $F$-statistic and corresponding $p$-value from the one-way ANOVA, respectively.

## 4.4 Computation of uncertainties

The uncertainty of the final $CO_2$ emission estimates was quantified by considering three independent sources: instrumental errors ($\delta_M$), wind measurement uncertainty ($\delta_V$), and thermodynamic variability associated with temperature and pressure ($\delta_{dens}$). These contributions were combined in quadrature:

$$\delta^2 = \delta_M^2 + \delta_V^2 + \delta_{dens}^2 \tag{4.7}$$

Table 6 presents all mean uncertainties of the $CO_2$ emissions calculated for the morning, noon, and evening periods in four seasons.

**Table 6.** Mean uncertainties (%) of $CO_2$ emissions derived from the UAV for four seasons. Columns labeled M, N, and E correspond to morning, noon, and evening periods, respectively. The total mean uncertainty $\delta$ is obtained by combining the individual contributions in quadrature for each period.

| | Spring | | | Summer | | | Autumn | | | Winter | | |
|---|---|---|---|---|---|---|---|---|---|---|---|---|
| | M | N | E | M | N | E | M | N | E | M | N | E |

| | | | | | | | | | | | | |
|---|---|---|---|---|---|---|---|---|---|---|---|---|
| $\delta_M$ | 2 | 1 | 1 | 2 | 2 | 3 | 2 | 2 | 1 | 2 | 5 | 1 |
| $\delta_V$ | 8 | 18 | 11 | 19 | 13 | 12 | 18 | 22 | 9 | 9 | 12 | 14 |
| $\delta_{dens}$ | 0 | 1 | 0 | 1 | 2 | 1 | 1 | 2 | 1 | 1 | 1 | 0 |
| $\delta$ | 8 | 18 | 11 | 19 | 13 | 12 | 18 | 22 | 9 | 9 | 13 | 14 |

889

890 ### 4.4.1 Instrumental errors

891 Instrumental errors are comparatively small. The ultrasonic anemometer used on
892 the UAV has a wind speed accuracy of ±0.2 m $s^{-1}$ and a wind direction accuracy of ±1°.
893 For typical flight-level wind speeds of 4-6 m $s^{-1}$, this corresponds to a relative error of
894 about 5% in the horizontal wind components. The closed-path $CO_2$ analyzer has an
895 accuracy of better than 0.2 ppm, whereas the plume enhancements resolved in the box
896 walls frequently exceed tens of ppm (e.g. up to ~40 ppm in the morning box on 8 August;
897 Fig. 11), implying a relative $CO_2$ uncertainty of approximately 0.5%. Propagating these
898 errors through the flux equations indicates that the instrumental contribution to the
899 emission rate uncertainty is generally below 5%, with a maximum of about 5%
900 uncertainty shown in Table 6. This contribution is therefore considered minor compared
901 to sampling and methodological effects.

902

903 ### 4.4.2 Wind measurement uncertainties

904 Uncertainty associated with wind measurements includes uncertainties arising
905 from sensor performance and interferences from UAV platform geometry-induced flow
906 distortion, UAV attitude changes during flight, as well as UAV flight speeds, and the
907 subsequent wind-correction procedure that was used to correct for these interferences.
908 The wind-correction algorithm, derived from extensive CFD simulations and in-flight
909 validation (Yang et al., 2025), corrects for rotor downwash, UAV attitude changes, and
910 background wind over a wide flight envelope conditions. Residual biases are most
911 likely during periods of strong turbulence or rapid maneuvers, but the close agreement
912 between UAV-derived friction velocity and flux tower estimates (Fig. 6b) suggests that
913 any remaining systematic error in wind speed is modest. Table 6 shows the mean
914 uncertainty for the $E_c$ term associated with wind measurements is estimated at 0.15 kg
915 $h^{-1}$ (8% of $E_c$, minimal impact) for the spring morning flight and 0.73 kg $h^{-1}$ (22%,

maximum impact) for the autumn noon flight. A conservative $\delta_V$ ≈8-22% is assigned to this uncertainty term.

### 4.4.3 Temperature and pressure impacts

The horizontal emission term in Eq. (3.4) depends explicitly on air density, which is determined by air temperature and pressure. In this study, the time-averaged temperature and pressure over the duration of each box-profile pair were used to derive a representative air density for the corresponding control volume. To assess the impact of temporal variability in the atmospheric thermodynamic conditions, the emission calculations were repeated using the minimum and maximum air densities observed during each flight period as alternative scenarios. As shown in Table 6, the resulting uncertainty associated with density variations is small ($\delta_{dens}$ ≈1-2%) and therefore represents only a minor contribution relative to the other uncertainty terms.

### 4.4.4 Total estimated uncertainties

By combining the uncertainties from the three independent components - instrumental errors ($\delta_M$), wind measurement uncertainties ($\delta_V$), and thermodynamic (temperature–pressure) variability ($\delta_{dens}$) - the total relative uncertainty of the UAV-derived $CO_2$ emission rates can be obtained through quadrature addition. As shown in Table 6, the total uncertainty typically falls within 8-22%, with the exact magnitude depending on atmospheric stability, time of day, and season. It should be noted that this uncertainty estimate primarily reflects measurement and propagation of errors within the flux calculation framework, and does not explicitly account for additional uncertainties associated with assumptions of stationarity, spatial interpolation, or unresolved sub-grid variability.

## 5 Conclusions

This study developed and field-evaluated a UAV-based methodology to quantify

three-dimensional $CO_2$ transport over a forest ecosystem by explicitly resolving both vertical exchange and horizontal advection within a three-dimensionally unified mass-balance approach, making use of an integrated UAV measurement platform and a computational algorithm that evaluates both horizontal and vertical fluxes based on a specifically designed flight strategy. Extensive applications of this methodology at the Qianyanzhou subtropical plantation forest site demonstrate that the methodology can robustly determine canopy-scale $CO_2$ exchange. Vertical $CO_2$ fluxes derived from UAV vertical profiles are in good agreement with those determined from collocated eddy covariance (EC) flux tower observations across seasons, with a Pearson correlation coefficient of $r$= 0.900, indicating that the UAV-based gradient method reproduces both the magnitude and variability of vertical turbulent exchange under typical daytime conditions. The UAV-based vertical fluxes showed clear diurnal and seasonal patterns over the forest ecosystem at Qianyanzhou, with the strongest uptake around midday during the growing season and near-neutral exchange in winter. However, vertical fluxes of UAV and EC diverge under weak turbulence during the evening stable period, highlighting increased uncertainties for both profile-based retrievals and tower-based estimates under low vertical flux conditions.

Box-pattern UAV measurements further reveal that horizontal transport can be a dominant term under certain conditions. Enhanced $CO_2$ concentrations on the virtual walls of the flight boxes and wind vectors show pronounced spatial heterogeneity and lateral gradients, especially in the morning, indicating that advection-driven convergence/divergence may substantially shape the local $CO_2$ budget, processes that cannot be directly resolved from single-tower measurements. A multi-scale analysis using different box sizes (50×50×50, 100×100×50, and 150×150×50 $m^3$) shows that net emission estimates can exhibit scale dependence, reflecting the spatial heterogeneity of sources/sinks. These results highlight the value of UAV observations for determining spatial heterogeneity in short term ecosystem carbon exchange with the atmosphere, a task unfit for single-site measurements, for diagnosing when and where the assumption of horizontal homogeneity becomes invalid, and for quantifying lateral flux

contributions explicitly.

Overall, the combined box-profile UAV framework provides a flexible and spatially explicit complement to conventional EC monitoring, offering an effective pathway to bridge the observational gap between point-scale tower fluxes and larger-scale heterogeneities, particularly over heterogeneous canopies and complex terrain. In conclusion, UAV-based platforms offer a transformative opportunity for observing ecosystem-atmosphere $CO_2$ exchange in three dimensions. With continued methodological refinement and broader application, such systems are well positioned to become an essential component of next-generation carbon observation strategies in forest ecosystems and beyond.

*Data availability*. Data are available upon request to the corresponding author upon reasonable request.

*Author contributions.* HS built the unmanned aerial vehicle platform, developed the corresponding emission inversion model, and carried out the data processing, and drafted the initial version of the manuscript. SML supervised the development of the inversion model and the experimental validation in the paper, and carried out a second round of revisions to the manuscript. YW provided some key data used in the paper. YY and TH provided the wind speed correction method used in the inversion model and the validation results for horizontal emissions, respectively. KC, CL, and JZ provided assistance with the field observation experiments and revisions to the manuscript. ZM and FY provided all flux tower data from the Qianyanzhou station. JG and XG provided support for unmanned aerial vehicle flights.

*Competing interests*. The contact author has declared that none of the authors has any competing interests.

*Disclaimer*. Publisher's note: Copernicus Publications remains neutral with regard to

jurisdictional claims made in the text, published maps, institutional affiliations, or any other geographical representation in this paper. While Copernicus Publications makes every effort to include appropriate place names, the final responsibility lies with the authors.

*Financial support*. This research has been supported by the National Key Research and Development Program of China, “Research on NQI Collaborative Innovation and Generic Key Technologies and Equipment to Support the Improvement of Data Quality for Carbon Trading” (2024YFF0618500).

# References


Aubinet, M., Heinesch, B., and Longdoz, B.: Estimation of the carbon sequestration by a heterogeneous forest: night flux corrections, heterogeneity of the site and inter-annual variability, Global Change Biology, 8, 1053-1071, https://doi.org/10.1046/j.1365-2486.2002.00529.x, 2002.

Aubinet, M., Vesala, T., and Papale, D. (Eds.): Eddy Covariance: A Practical Guide to Measurement and Data Analysis, Springer, Dordrecht, 2012.

Baldocchi, D.: Breathing of the terrestrial biosphere: lessons learned from a global network of carbon dioxide flux measurement systems, Australian Journal of Botany, 56, 1-26, https://doi.org/10.1071/bt07151, 2008.

Baldocchi, D., Falge, E., Gu, L. H., Olson, R., Hollinger, D., Running, S., Anthoni, P., Bernhofer, C., Davis, K., Evans, R., Fuentes, J., Goldstein, A., Katul, G., Law, B., Lee, X. H., Malhi, Y., Meyers, T., Munger, W., Oechel, W., U, K. T. P., Pilegaard, K., Schmid, H. P., Valentini, R., Verma, S., Vesala, T., Wilson, K., and Wofsy, S.: FLUXNET: A new tool to study the temporal and spatial variability of ecosystem-scale carbon dioxide, water vapor, and energy flux densities, Bulletin of the American Meteorological Society, 82, 2415-2434, https://doi.org/10.1175/1520-0477(2001)082<2415:Fantts>2.3.Co;2, 2001.

Baldocchi, D. D.: Assessing the eddy covariance technique for evaluating carbon dioxide exchange rates of ecosystems: past, present and future, Global Change Biology, 9, 479-492, https://doi.org/10.1046/j.1365-2486.2003.00629.x, 2003.

Bolek, A., Heimann, M., and Göckede, M.: UAV-based in situ measurements of $CO_2$ and $CH_4$ fluxes over complex natural ecosystems, Atmospheric Measurement Techniques, 17, 5619-5636, https://doi.org/10.5194/amt-17-5619-2024, 2024.

Bonan, G. B.: Forests and climate change: Forcings, feedbacks, and the climate benefits of forests, Science, 320, 1444-1449, https://doi.org/10.1126/science.1155121, 2008.

Budyko, M. I., Yefimova, N. A., Aubenok, L. I., and L. A. Strokina: The heat balance of the earth's surface, Soviet Geography, 5, 3-16, https://doi.org/10.1080/00385417.1962.10769936, 1962.

Burba, G. G., Schmidt, A., Scott, R. L., Nakai, T., Kathilankal, J. C., Fratini, G., Hanson, C.,: Calculating $CO_2$ and $H_2O$ eddy covariance fluxes from an enclosed gas analyzer using an instantaneous mixing ratio approach. Global Change Biology, 18, 385–399, https://doi.org/10.1111/j.1365-2486.2011.02536.x, 2012.

Burman, P. K. D., Bhat, G. S., Tiwari, Y. K., Morrison, R., Rodda, S. R., Mukherjee, S., Dadhwal, V. K., Turner, A. G., Das, P., Agarwal, G., Sarma, D., Mutyala, P., Gogoi, N., Gnanamoorthy, P., Paleri, S., Desai, D.: Ecosystem-atmosphere exchanges of carbon dioxide, water vapour and energy in India: A synthesis of insights from eddy covariance measurements. Agricultural and Forest Meteorology, 372, 110730, https://doi.org/10.1016/j.agrformet.2025.110730, 2025.

Cambaliza, M. O. L., Shepson, P. B., Caulton, D. R., Stirm, B., Samarov, D., Gurney, K. R., Turnbull, J., Davis, K. J., Possolo, A., Karion, A., Sweeney, C., Moser, B., Hendricks, A., Lauvaux, T., Mays, K., Whetstone, J., Huang, J., Razlivanov, I., Miles, N. L., and Richardson, S. J.: Assessment of uncertainties of an aircraft-based mass balance approach for quantifying urban greenhouse gas emissions, Atmospheric Chemistry and Physics, 14, 9029-9050, https://doi.org/10.5194/acp-14-9029-2014, 2014.

Chevallier, F., Palmer, P. I., Feng, L., Boesch, H., O'Dell, C. W., and Bousquet, P.: Toward robust and consistent regional $CO_2$ flux estimates from in situ and spaceborne measurements of atmospheric

$CO_2$, Geophysical Research Letters, 41, 1065-1070, https://doi.org/10.1002/2013gl058772, 2014.
Crisp, D., Pollock, H. R., Rosenberg, R., Chapsky, L., Lee, R. A. M., Oyafuso, F. A., Frankenberg, C., O'Dell, C. W., Bruegge, C. J., Doran, G. B., Eldering, A., Fisher, B. M., Fu, D. J., Gunson, M. R., Mandrake, L., Osterman, G. B., Schwandner, F. M., Sun, K., Taylor, T. E., Wennberg, P. O., and Wunch, D.: The on-orbit performance of the Orbiting Carbon Observatory-2 (OCO-2) instrument and its radiometrically calibrated products, Atmospheric Measurement Techniques, 10, 59-81, https://doi.org/10.5194/amt-10-59-2017, 2017.
Fang, J., Fang, J., Chen, B., Zhang, H., Dilawar, A., Guo, M., & Liu, S.: Assessing Spatial Representativeness of Global Flux Tower Eddy-Covariance Measurements Using Data from FLUXNET2015, Scientific Data, 11, 569, https://doi.org/10.1038/s41597-024-03291-3, 2024.
Feigenwinter, C., Bernhofer, C., and Vogt, R.: The influence of advection on the short term $CO_2$-budget in and above a forest canopy, Boundary-Layer Meteorology, 113, 201-224, https://doi.org/10.1023/B:BOUN.0000039372.86053.ff, 2004.
Finnigan, J. J., Clement, R., Malhi, Y., Leuning, R., and Cleugh, H. A.: A re-evaluation of long-term flux measurement techniques - Part I: Averaging and coordinate rotation, Boundary-Layer Meteorology, 107, 1-48, https://doi.org/10.1023/a:1021554900225, 2003.
Foken, T.: The energy balance closure problem: An overview, Ecological Applications, 18, 1351-1367, https://doi.org/10.1890/06-0922.1, 2008.
Gioli, B., Miglietta, F., De Martino, B., Hutjes, R. W. A., Dolman, H. A. J., Lindroth, A., Schumacher, M., Sanz, M. J., Manca, G., Peressotti, A., and Dumas, E. J.: Comparison between tower and aircraft-based eddy covariance fluxes in five European regions, Agricultural and Forest Meteorology, 127, 1-16, https://doi.org/10.1016/j.agrformet.2004.08.004, 2004.
Gordon, M., Li, S. M., Staebler, R., Darlington, A., Hayden, K., O'Brien, J., and Wolde, M.: Determining air pollutant emission rates based on mass balance using airborne measurement data over the Alberta oil sands operations, Atmospheric Measurement Techniques, 8, 3745-3765, https://doi.org/10.5194/amt-8-3745-2015, 2015.
Goulden, M. L., Munger, J. W., Fan, S. M., Daube, B. C., and Wofsy, S. C.: Measurements of carbon sequestration by long-term eddy covariance: Methods and a critical evaluation of accuracy, Global Change Biology, 2, 169-182, https://doi.org/10.1111/j.1365-2486.1996.tb00070.x, 1996.
Han, T. R., Xie, C. H., Liu, Y. Y., Yang, Y. R., Zhang, Y. H., Huang, Y. F., Gao, X. Y., Zhang, X. H., Bao, F. M., and Li, S. M.: Development of a continuous UAV-mounted air sampler and application to the quantification of $CO_2$ and $CH_4$ emissions from a major coking plant, Atmospheric Measurement Techniques, 17, 677-691, https://doi.org/10.5194/amt-17-677-2024, 2024.
Huang, M., Ji, J. J., Li, K. R., Liu, Y. F., Yang, F. T., and Tao, B.: The ecosystem carbon accumulation after conversion of grasslands to pine plantations in subtropical red soil of south China, Tellus Series B-Chemical and Physical Meteorology, 59, 439-448, https://doi.org/10.1111/j.1600-0889.2007.00280.x, 2007.
IPCC: Climate Change 2021: The Physical Science Basis., Contribution of Working Group I to the Sixth Assessment Report of the IPCC., Cambridge University Press., https://doi.org/10.1017/9781009157896, 2021.
Jacob, D. J., Turner, A. J., Maasakkers, J. D., Sheng, J. X., Sun, K., Liu, X., Chance, K., Aben, I., McKeever, J., and Frankenberg, C.: Satellite observations of atmospheric methane and their value for quantifying methane emissions, Atmospheric Chemistry and Physics, 16, 14371-14396, https://doi.org/10.5194/acp-16-14371-2016, 2016.

Jung, M., Schwalm, C., Migliavacca, M., Walther, S., Camps-Valls, G., Koirala, S., Anthoni, P., Besnard, S., Bodesheim, P., Carvalhais, N., Chevallier, F., Gans, F., Goll, D. S., Haverd, V., Köhler, P., Ichii, K., Jain, A. K., Liu, J. Z., Lombardozzi, D., Nabel, J., Nelson, J. A., O'Sullivan, M., Pallandt, M., Papale, D., Peters, W., Pongratz, J., Rödenbeck, C., Sitch, S., Tramontana, G., Walker, A., Weber, U., and Reichstein, M.: Scaling carbon fluxes from eddy covariance sites to globe: synthesis and evaluation of the FLUXCOM approach, Biogeosciences, 17, 1343-1365, https://doi.org/10.5194/bg-17-1343-2020, 2020.

Kaimal, J. C. and Finnigan, J. J.: Atmospheric Boundary Layer Flows: Their Structure and Measurement, Oxford University Press, Oxford, 1994.

Khan, A., Schaefer, D., Tao, L., Miller, D. J., Sun, K., Zondlo, M. A., Harrison, W. A., Roscoe, B., and Lary, D. J.: Low Power Greenhouse Gas Sensors for Unmanned Aerial Vehicles, Remote Sensing, 4, 1355-1368, https://doi.org/10.3390/rs4051355, 2012.Langelaan, J. W., Alley, N., and Neidhoefer, J.: Wind field estimation for small unmanned aerial vehicles, Journal of Guidance Control and Dynamics, 34, 1016-1030, https://doi.org/10.2514/1.52532, 2011.

Lee, Y. H. and Mahrt, L.: Effect of stability on mixing in open canopies, Agricultural and Forest Meteorology, 135, 169–179, https://doi.org/10.1016/j.agrformet.2005.11.013, 2005.

Leuning, R., Cleugh, H. A., Zegelin, S. J., and Hughes, D.: Carbon and water fluxes over a temperate Eucalyptus forest and a tropical wet/dry savanna in Australia: measurements and comparison with MODIS remote sensing estimates, Agricultural and Forest Meteorology, 129, 151-173, https://doi.org/10.1016/j.agrformet.2004.12.004, 2005.

Leuning, R., Zegelin, S. J., Jones, K., Keith, H., and Hughes, D.: Measurement of horizontal and vertical advection of $CO_2$ within a forest canopy, Agricultural and Forest Meteorology, 148, 1777-1797, https://doi.org/10.1016/j.agrformet.2008.06.006, 2008.

Mahrt, L.: Flux sampling errors for aircraft and towers, Journal of Atmospheric and Oceanic Technology, 15, 416-429, https://doi.org/10.1175/1520-0426(1998)015<0416:Fsefaa>2.0.Co;2, 1998.

Mahrt, L.: Variability and Maintenance of Turbulence in the Very Stable Boundary Layer, Boundary-Layer Meteorology, 135, 1-18, https://doi.org/10.1007/s10546-009-9463-6, 2010.

Meredith L. K., Commane R., Munger J. W., Dunn, A., Tang, J., Wofsy, S. C., and Prinn R. G.: Ecosystem fluxes of hydrogen: a comparison of flux-gradient methods, Atmospheric Measurement Techniques, 7(9): 2787-2805, https://doi.org/10.5194/amt-7-2787-2014, 2014.

Metzger, S., Durden, D., Sturtevant, C., Desai, A. R., Li, J. H.; Luo, H. Y., and Zulueta, R. C.: Optimization of an enclosed gas analyzer sampling system for measuring eddy covariance fluxes of $H_2O$ and $CO_2$. Atmospheric Measurement Techniques, 9, 1341–1359, https://doi.org/10.5194/amt-9-1341-2016, 2016.

Monin, A. S. and Obukhov, A. M.: Basic laws of turbulent mixing in the surface layer of the atmosphere, Trudy Geophys. Inst. AN. SSSR, 24, 153-187, 1954.

Niedzielski, T., Skjoth, C., Werner, M., Spallek, W., Witek, M., Sawinski, T., Drzeniecka-Osiadacz, A., Korzystka-Muskala, M., Muskala, P., Modzel, P., Guzikowski, J., and Kryza, M.: Are estimates of wind characteristics based on measurements with Pitot tubes and GNSS receivers mounted on consumer-grade unmanned aerial vehicles applicable in meteorological studies?, Environmental Monitoring and Assessment, 189, https://doi.org/10.1007/s10661-017-6141-x, 2017.

Nolan, P. J., Pinto, J., González-Rocha, J., Jensen, A., Vezzi, C. N., Bailey, S. C. C., de Boer, G., Diehl, C., Laurence, R., Powers, C. W., Foroutan, H., Ross, S. D., and Schmale, D. G.: Coordinated unmanned aircraft system (UAS) and ground-based weather measurements to predict lagrangian

coherent structures (LCSs), Sensors, 18, https://doi.org/10.3390/s18124448, 2018.
Palomaki, R. T., Rose, N. T., van den Bossche, M., Sherman, T. J., and De Wekker, S. F. J.: Wind estimation in the lower atmosphere using multirotor aircraft, Journal of Atmospheric and Oceanic Technology, 34, 1183-1191, https://doi.org/10.1175/jtech-d-16-0177.1, 2017.
Pan, Y. D., Birdsey, R. A., Fang, J. Y., Houghton, R., Kauppi, P. E., Kurz, W. A., Phillips, O. L., Shvidenko, A., Lewis, S. L., Canadell, J. G., Ciais, P., Jackson, R. B., Pacala, S. W., McGuire, A. D., Piao, S. L., Rautiainen, A., Sitch, S., and Hayes, D.: A Large and Persistent Carbon Sink in the World's Forests, Science, 333, 988-993, https://doi.org/10.1126/science.1201609, 2011.
Pastorello, G., Trotta, C., Canfora, E., Chu, H. S., Christianson, D., Cheah, Y. W., Poindexter, C., Chen, J. Q., Elbashandy, A., Humphrey, M.:The FLUXNET2015 dataset and the ONEFlux processing pipeline for eddy covariance data. Scientific Data, 7, 225, https://doi.org/10.1038/s41597-020-0534-3, 2020.
Raupach, M. R.: Simplified expressions for vegetation roughness length and zero-plane displacement as functions of canopy height and area index. Boundary-Layer Meteorology, 71, 211–216, https://doi.org/ 10.1007/BF00709229, 1994.Rogers, K. and Finn, A.: Three-dimensional UAV-based atmospheric tomography, Journal of Atmospheric and Oceanic Technology, 30, 336-344, https://doi.org/10.1175/jtech-d-12-00036.1, 2013.
Sahlée, E., Smedman, A.-S., Högström, U., and Rutgersson, A.: Reevaluation of the bulk exchange coefficient for humidity at sea during unstable and neutral conditions, Journal of Physical Oceanography, 38, 257-272, https://doi.org/10.1175/2007JPO3754.1, 2008.
Schimel, D., Pavlick, R., Fisher, J. B., Asner, G. P., Saatchi, S., Townsend, P., Miller, C., Frankenberg, C., Hibbard, K., and Cox, P.: Observing terrestrial ecosystems and the carbon cycle from space, Global Change Biology, 21, 1762-1776, https://doi.org/10.1111/gcb.12822, 2015.
Schmid, H. P.: Footprint modeling for vegetation atmosphere exchange studies: a review and perspective, Agricultural and Forest Meteorology, 113, 159-183, https://doi.org/10.1016/s0168-1923(02)00107-7, 2002.
Shimura, T., Inoue, M., Tsujimoto, H., Sasaki, K., and Iguchi, M.: Estimation of wind vector profile using a hexarotor unmanned aerial vehicle and its application to meteorological observation up to 1000 m above surface, Journal of Atmospheric and Oceanic Technology, 35, 1621-1631, https://doi.org/10.1175/jtech-d-17-0186.1, 2018.
Smith, R. J.: Use and Misuse of the Reduced Major Axis for Line-Fitting, American Journal of Physical Anthropology, 140, 476-486, https://doi.org/10.1002/ajpa.21090, 2009.
Soddell, J. R., McGuffie, K., and Holland, G. J.: Intercomparison of atmospheric soundings from the aerosonde and radiosonde, Journal of Applied Meteorology, 43, 1260-1269, https://doi.org/10.1175/1520-0450(2004)043<1260:Ioasft>2.0.Co;2, 2004.
Soltaninezhad, M., Monsorno, R., and Tondini, S.: A Review of Methods and Challenges for Wind Measurement by Small Unmanned Aerial Vehicles, Meteorological Applications, 32, https://doi.org/10.1002/met.70065, 2025.
Spiess, T., Bange, J., Buschmann, M., and Vörsmann, P.: First application of the meteorological Mini-UAV 'M2AV', Meteorologische Zeitschrift, 16, 159-169, https://doi.org/10.1127/0941-2948/2007/0195, 2007.
Stull, R. B.: An Introduction to Boundary Layer Meteorology, Kluwer Academic Publishers, Dordrecht, 1988.
Thielicke, W., Hübert, W., Müller, U., Eggert, M., and Wilhelm, P.: Towards accurate and practical drone-

based wind measurements with an ultrasonic anemometer, Atmospheric Measurement Techniques, 14, 1303-1318, https://doi.org/10.5194/amt-14-1303-2021, 2021.

Vickers, D. and Mahrt, L.: Quality control and flux sampling problems for tower and aircraft data, Journal of Atmospheric and Oceanic Technology, 14, 512-526, https://doi.org/10.1175/1520-0426(1997)014<0512:QCAFSP>2.0.CO;2, 1997.

Villa, T. F., Salimi, F., Morton, K., Morawska, L., and Gonzalez, F.: Development and Validation of a UAV Based System for Air Pollution Measurements, Sensors, 16, https://doi.org/10.3390/s16122202, 2016.

Warton, D. I., Wright, I. J., Falster, D. S., and Westoby, M.: Bivariate line-fitting methods for allometry, Biological Reviews, 81, 259-291, https://doi.org/10.1017/s1464793106007007, 2006.

Webb, E. K., Pearman, G. I., & Leuning, R.: Correction of flux measurements for density effects due to heat and water vapour transfer. Quarterly Journal of the Royal Meteorological Society, 106, 85–100, https://doi.org/10.1002/qj.49710644707, 1980.Wilson, K., Goldstein, A., Falge, E., Aubinet, M., Baldocchi, D., Berbigier, P., Bernhofer, C., Ceulemans, R., Dolman, H., Field, C., Grelle, A., Ibrom, A., Law, B. E., Kowalski, A., Meyers, T., Moncrieff, J., Monson, R., Oechel, W., Tenhunen, J., Valentini, R., and Verma, S.: Energy balance closure at FLUXNET sites, Agricultural and Forest Meteorology, 113, 223-243, https://doi.org/10.1016/s0168-1923(02)00109-0, 2002.

Witte, B. M., Singler, R. F., and Bailey, S. C. C.: Development of an Unmanned Aerial Vehicle for the Measurement of Turbulence in the Atmospheric Boundary Layer, Atmosphere, 8, https://doi.org/10.3390/atmos8100195, 2017.

WMO: Greenhouse Gas concentrations hit record high. Again., press release, 15 November 2023, available at: https://wmo.int/news/media-centre/greenhouse-gas-concentrations-hit-record-high-again, last access: 28 January 2026, 2023.

Yang, Y. R., Zhang, Y. H., Han, T. R., Xie, C. H., Liu, Y. Y., Huang, Y. F., Zhou, J. T., Sun, H. J., Zhao, D. L., Zhang, K., and Li, S. M.: A correction algorithm for rotor-induced airflow and flight attitude changes during three-dimensional wind speed measurements made from a rotary unoccupied aerial vehicle, Atmospheric Measurement Techniques, 18, 3035-3050, https://doi.org/10.5194/amt-18-3035-2025, 2025.

Yu, G. R., Wen, X. F., Sun, X. M., Tanner, B. D., Lee, X. H., and Chen, J. Y.: Overview of ChinaFLUX and evaluation of its eddy covariance measurement, Agricultural and Forest Meteorology, 137, 125-137, https://doi.org/10.1016/j.agrformet.2006.02.011, 2006.

Yu, G. R., Zhang, L. M., Sun, X. M., Fu, Y. L., Wen, X. F., Wang, Q. F., Li, S. G., Ren, C. Y., Song, X., Liu, Y. F., Han, S. J., and Yan, J. H.: Environmental controls over carbon exchange of three forest ecosystems in eastern China, Global Change Biology, 14, 2555-2571, https://doi.org/10.1111/j.1365-2486.2008.01663.x, 2008.

Zhang, S. P., Yi, X., Zheng, X. G., Chen, Z. Q., Dan, B., and Zhang, X. Z.: Global carbon assimilation system using a local ensemble Kalman filter with multiple ecosystem models, Journal of Geophysical Research-Biogeosciences, 119, 2171-2187, https://doi.org/10.1002/2014jg002792, 2014.